Integrated Pliocene-Pleistocene magnetostratigraphy and tephrostratigraphy of deep-sea sediments at IODP Site U1424 (Yamato Basin, Japan Sea)

Chuang Xuan [1]
Corresponding author
Email: c.xuan@soton.ac.uk

Yuxi Jin [1]
Email: y.jin@soton.ac.uk

Saiko Sugisaki [2]
Email: s.sugisaki@aist.go.jp

Yasufumi Satoguchi [3]
Email: satoguchi-yasufumi@biwahaku.jp

Yoshitaka Nagahashi [4]
Email: nagahashi@sss.fukushima-u.ac.jp

[1] School of Ocean and Earth Science, National Oceanography Centre Southampton, University of Southampton, Waterfront Campus, European Way, Southampton, SO14 3ZH, UK

[2] Research Institute of Geology and Geoinformation, Geological Survey of Japan, AIST, Central 7, 1-1-1 Higashi, Tsukuba 305-8567, Japan

[3] Lake Biwa Museum, 1091 Oroshimo, Kusatsu, Shiga, 525-0001, Japan

[4] Faculty of Symbiotic Systems Science, Fukushima University, 1 Kanayagawa, Fukushima, Fukushima, 960-1296, Japan

Abstract

Sediments from the semi-enclosed Japan Sea are sensitive to paleoclimatic perturbations and they offer great opportunities for many regional and global paleoceanographic and paleoclimatic studies. These studies often require a robust chronology. However, due to rare preservation of calcareous microfossils and drastic changes in surface water salinity during glacial lowstands, the construction of a traditional oxygen isotope stratigraphy for Japan Sea sediments is often difficult. Here, we use sediments recovered at Integrated Ocean Drilling Program (IODP) Expedition 346 Site U1424 to build an integrated Pliocene-Pleistocene reference magnetostratigraphy and tephrostratigraphy for sedimentary sequences from the region. Rock magnetic experiments indicate that magnetic remanence of Site U1424 sediments are carried primarily by (titano)magnetite with small contributions from high coercivity minerals (e.g. hematite) and possibly iron sulphides (pyrrhotite and/or greigite). Dark-colored sediments appear to contain less (titano)magnetite probably due to reductive diagenesis under euxinic conditions. Natural remanent magnetization (NRM) of u-channel samples covering a continuous ~167.6 m sediment sequence at Site U1424 were repeatedly measured at 1-cm intervals before and after stepwise demagnetization. Despite lower NRM intensity in dark-colored sediments, NRM directional data from both dark- and light-colored sediments are considered suitable for the construction of magnetostratigraphy. Site U1424 sediments clearly recorded the majority of the polarity Chrons and subchrons within the last ~4.89 Myr, with the Cobb Mountain subchron, the end of Kaena subchron, and the onset of Nunivak subchron less well preserved. Sixteen tephra layers from the site were sampled for chemical composition analyses and the results were correlated to reference tephrostratigraphy of the region. Ages of the identified tephras are consistent with and can be well integrated with the magnetostratigraphy. The resulting age model suggests that sedimentation rates at Site U1424 range between ~1.7 and 7.6 cm/kyr with an average of ~3.3 cm/kyr. The acquired magnetostratigraphy and tephrostratigraphy at Site U1424 provide a reference chronology that can be correlated with and transferred to other sediment sequences in the region to study paleoceanographic and paleoclimatic changes of the region as well as their links to other regional and global changes.

Keywords

Paleomagnetism, magnetostratigraphy, tephrostratigraphy, Japan Sea, IODP Expedition 346, Site U1424

Introduction

The Japan Sea is a semi-enclosed marginal sea located on the eastern end of the Asian continent with an average depth of ~1350 m and it covers an area of about one million square kilometers. It is connected to other seas only through narrow and shallow straits with present sill depth of ~130 m (Fig. 1). The Japan Sea has been responding to changes of global surface conditions in sensitive manner at various time scales since it was formed at ~20 Ma (Tada 1994). Deposition of sediments and euxinic conditions in the Japan Sea were largely modulated by paleoceanographic conditions which were strongly influenced by factors such as sill depth, position of channels, and the degree of closure of the sea. These factors were controlled by local tectonism and/or global eustatic sea level changes (Tada 1994). Sedimentary records from the Japan sea provide great opportunity to study paleoceanographic and paleoclimatic changes of the region as well as their links to other regional and global processes. For example, studies on cores recovered by Ocean Drilling Program (ODP) Legs 127/128 (Tamaki et al. 1990; Ingle et al. 1990; Tada et al. 1992) show that Quaternary sediments in deeper part of the Japan Sea are characterised by centimeter- to meter-scale alternations of dark organic-rich layers and light organic-poor layers. The alternations of dark and light layers were demonstrated to record wet and dry cycles in central to eastern Asia that could be linked to Dansgaard–Oeschger cycles with dark layers deposited during interstadials (Tada et al. 1999; Tada, 2005; Tada 2012). Marine sediments in the Japan Sea also hold great potential to build long and continuous records that are key to understanding land-ocean linkages and interrelationships between East Asian

Summer/Winter Monsoon and the Westerly Jet axis movement through the Pliocene-Pleistocene (Tada et al. 2013).

In 2013, Integrated Ocean Drilling Program (IODP) Expedition 346 (Asian Monsoon) drilled at seven sites in the Japan Sea and two sites in the East China Sea (Fig. 1) (Expedition 346 Scientists 2014). The overall goal of the Expedition was to test the relationship between uplift of the Tibetan plateau, Westerly Jet circulation, and evolution of the East Asian monsoon. A fundamental requirement for these studies is a robust chronology for the recovered sediments so that timing, duration, and rates of change for events and processes revealed by various proxy records could be determined. However, construction of traditional oxygen isotope stratigraphy for Japan Sea sediments is challenging due to rare preservation of calcareous microfossils and drastic changes in surface water salinity during some glacial lowstands (Oba et al. 1991). The construction of chronology for Pliocene-Pleistocene sediments from the Japan Sea often rely on magnetostratigraphy and tephrostratigraphy (see Hamano et al. 1992; Tada 1994; Tada et al. 2018). Magnetostratigraphy of ODP Leg 127/128 sediments from the Japan Sea mainly relied on shipboard half-core section measurement made at low resolution (i.e. 10 cm interval) and a very limited number of discrete cube samples (see Hamano et al. 1992). However, reasonable quality polarity records were acquired mostly for sediments within the last ~2.5 Myr cored using advanced piston corer (APC) from a single hole (see Tada 1994).

Site U1424 drilled during IODP Expedition 346 was used as a chronology reference record by Tada et al. (2018) to build a “paleo-observatory network”, which comprises sediment archives from six sites drilled in the Japan Sea during IODP Expedition 346. These sites cover wide ranges of latitudes, longitudes, and water depths and allow the reconstruction of temporal-spatial changes in material fluxes in the Japan Sea. Detailed correlation of dark layers in the sediments guided by magnetostratigraphy and tephrostratigraphy was used by the authors to project the Site U1424 chronology to five other sites. The site U1424 chronology used by Tada et al. (2018) incorporated the best paleomagnetic and tephra data available at the time which covered the last ~3 Myr (see Table 1 in Tada et al. 2018), and was further tuned to the LR04 stack (Lisiecki and Raymo, 2005) using gamma ray attenuation density (GRA) and natural gamma radiation (NGR) data. Polarity reversals in Site U1424 sediments used by Tada et al. (2018) were determined based on partially demagnetized (using alternating fields with peak fields up to 30 mT) u-channel sample data available at the time (i.e. for sediments younger than ~3 Ma), and are more reliable and accurate than those acquired based on shipboard measurement (Tada et al. 2015).

In this paper, we report high-resolution magnetostratigraphy for Site U1424 sediments based on shore-based measurement of u-channel samples with complete sequence of stepwise demagnetization (with peak fields up to 100 mT). The analysed u-channel samples continuously cover the a total of ~167.6 m sediment sequence (spanning the last ~4.89 Myr) recovered at Site U1424. We conducted rock magnetic experiments to investigate the magnetic mineralogy of the sediments and to help verify the fidelity of the reconstructed paleomagnetic records. Chemical compositions of sixteen tephra layers from Site U1424 were analysed and reported here, and the studied tephra layers were correlated with Pliocene-Pleistocene reference tephrostratigraphy of the region. Note that an earlier version of the tephra correlation was used by Tada et al. (2018) to support their chronology for Site U1424 sediments of the last ~3 Myr. We compare and discuss results from the paleomagnetism and tephra studies conducted to form an integrated magnetostratigraphy and tephrostratigraphy for the sediment sequence cored at IODP Site U1424.

Samples and Methods

IODP Site U1424

IODP Site U1424 (40°11.40′N, 138°13.90′E, ~2808 m water depth) was drilled at the same location as ODP Site 794 and is located in the eastern part of the Yamato Basin, Japan Sea, ~200 km southwest of the Tsugaru Strait (Fig. 1). The site is mainly under the influence of the second branch of the Tsushima Warm Current (TWC). A total of 41 cores from three holes were recovered at Site U1424 using the advanced piston corer (APC). The recovered cores form a complete stratigraphic sequence of ~167.75 m of sediments (Tada et al. 2015).

Site U1424 sediments are dominated by clay and diatom ooze with minor component of pyrite and volcaniclastic materials (concentrated at numerous tephra layers) throughout the sediment succession (Tada et al. 2015). These sediments are divided into two major lithologic units: Units I and II, with the boundary at ~70 m core composite depth below sea floor (CCSF-A). Unit I sediments are characterized by alternating decimeter-scale color-banded bedding with dark, organic-rich clay intervals interspersed with lighter colored, organic-poor intervals. Unit I sediments are further divided into Subunits IA and IB (boundary at ~47.7 m CCSF-A).

Subunit IA is characterized by decimeter-scale alternations of light and dark colored sediment intervals and Subunit IB is identified by a decrease in the frequency of dark and light color alternation and the dominance of light greenish gray and light gray clay (Tada et al. 2015). Unit II is distinguished from Unit I on the basis of the sediment color and a significant increase in diatom content and is further divided into Subunits IIA and IIB (boundary at ~85 m CCSF-A). Subunit IIA is dominated by brownish and greenish diatom-bearing and diatom-rich clay, and Subunit IIB is defined by the consistent appearance of diatom ooze (Tada et al. 2015).

Paleomagnetic analysis of u-channel samples

A total of 143 continuous u-channel samples were collected for paleomagnetism studies. Sampling of the u-channels followed the shipboard splice derived from Holes U1424A and U1424B (see Table T18 in Tada et al. 2015). All u-channel samples were taken from the center part of the half-core sections to avoid disturbed core margins that can influence the quality of paleomagnetic records. Sample from Core-section U1424B-6H-5 was taken from the working-half of the core-section. All other samples were taken from archive-half core-sections. Sediments in each u-channel sample were enclosed in plastic container that has the same length as the core-section (typically ~150 cm) and an internal cross section of ~1.8×1.9 cm^2, with a clip-on plastic cover that seals the sediments to minimize dehydration (Tauxe et al. 1983). The collected u-channel samples cover a continuous sediment sequence between 0-167.6 m CCSF-A at IODP Site U1424.

Natural remanent magnetization (NRM) of the u-channel samples were measured on a 2G Enterprises liquid helium-cooled pass-through superconducting rock magnetometer (SRM) at the University of Southampton. The SRM has a narrow sample access bore (4.2-cm diameter) designed for u-channel measurements and is housed inside a magnetically shielded room. NRM measurements for each u-channel were made at 1-cm intervals over the sample length as well as over a 10-cm "leader" interval before the sample and a 10-cm "trailer" interval after the sample. The "leader" and "trailer" measurements serve the dual functions of monitoring the measurement background and allowing for future signal deconvolution (see Oda and Xuan 2014; Xuan and Oda 2015). NRM of all samples were repeatedly measured after progressive alternating field (AF) demagnetization with peak fields of 20-50 mT in 5 mT increments, and at 60, 80, and 100 mT (10 steps in total). For a few u-channel samples, NRM measurements were also collected after AF demagnetization with additional peak fields of 55, 65, 70, and 90 mT.

The UPmag software (Xuan and Channell 2009) was used to correct any flux jumps and spike noises in NRM measurements. We normalized all u-channel measurements using a nine-term "effective length" matrix estimated for the SRM to gain more accurate NRM intensity and directional data (see Xuan and Oda 2019). For each 1-cm interval, component magnetization directions were calculated using principal component analysis (PCA, Kirschvink 1980) and the UPmag software (Xuan and Channell 2009). PCA calculations used NRM data from 9 common steps between 20-80 mT demagnetization without anchoring the directions to the origin of the orthogonal projections. PCA results are associated with maximum angular deviation (MAD) values that monitor the quality of the definition of component directions. In addition, we calculated mean declinations and inclinations based on Fisher statistics for the same NRM data used in the PCA calculations. These mean directions are accompanied with α_{95} values that estimate the circle of 95% confidence about the mean directions. The α_{95} values complement the PCA MAD values and provide an additional check on NRM data quality. For example, NRM demagnetization data that lie closely on a line in vector space but not cross near the origin would yield a small MAD value, but such data would be associated with large α_{95} values (see van Peer et al. 2017). Declination data from each core were corrected by uniform rotation of each core so that the circular mean of the corrected declinations is oriented north or south for positive and negative inclination intervals, respectively. An additional 180° rotation was applied to correct declination data of the u-channel sample taken from the working-half of Core-section U1424B-6H-5.

Rock magnetic experiments

During u-channel sampling of some core-sections, excess sediments that stuck along the outside walls of the plastic u-channel containers were scraped and placed in plastic bags. The scrapings represent an average bulk sediment sample of the core-section (typically ~1.5 m long) from which the u-channel were taken. Selected scraping samples were used for rock magnetic experiments on a Princeton Measurements Corp. (now Lakeshore Inc.) Model 3900 vibrating sample magnetometer (VSM) at the University of Southampton. Weight of samples used for all analyses on the VSM was measured and used to normalize the measurement data.

Hysteresis loops for a group of samples were measured using applied fields ranging between -0.5 T and +0.5 T with steps of 4-5 mT and averaging time of 500-800 ms. For backfield experiments on the same samples, a 0.5-T field was first applied to the samples, remanence of the samples was then monitored after applying (and turning off) an increasing field (with a 2.5-mT increment) in the opposite direction until zero remanence was reached. Hysteresis loop data were processed, and slope corrected following the procedures of Jackson and Solheid (2010) and using the HystLab program (Paterson et al. 2018). The “Automatic” routine in HystLab was used to decide most suitable methods for both drift and slope corrections of data (see Paterson et al. 2018). The slope corrected hysteresis loop data and backfield curves were used to determine ratios of hysteresis parameters: Mr/Ms and Bcr/Bc, where Mr is saturation remanence, Ms is saturation magnetization, Bcr is coercivity of remanence, and Bc is coercivity.

Selected bulk samples were used for isothermal remanent magnetization (IRM) acquisition experiments on the VSM. IRM of the samples were acquired and measured (using averaging time of 500 ms) at 100 field steps on a logarithmic scale ranging from 0.1 mT to 1 T. In addition, two samples from Core U1424B-2H were used for first order reversal curve (FORC) measurements (Pike et al. 1999; Roberts et al. 2000, 2014) on the VSM. The FORC diagrams consist of 133 curves collected at 2 mT field increments with an averaging time of 200 ms. FORC measurement data were analyzed using the FORCinel software (Harrison and Feinberg 2008), which incorporates VARIFORC smoothing (Egli 2013) and statistical confidence intervals (Heslop and Roberts 2012).

Two samples from the top part of Hole U1424A (i.e. 1H-2W, 89-91 cm and 1H-4W, 94-96 cm) were measured on a low-temperature susceptometer (Quantum design MPMS-XL-5) at the Center for Advanced Marine Core Research (CMCR), Kochi University. The samples were first dried, then saturation IRM (SIRM) was imparted using a 3-T field at room temperature of 300 K. IRM of the samples were then monitored while the samples were cooled to 10 K and subsequently warmed to 300K in zero field. The samples were then cooled from 300 K to 10 K in zero field, and an IRM was imparted using a 3-T field at 10 K. The acquired IRM was then monitored while warming the samples to 300 K in zero field.

Color data from half-core section photos

To check if any relationship exists between NRM data and sediment color, we stacked half-core section image (using the "trimmed" version) scanned onboard *JOIDES Resolution* during IODP Expedition 346 (Tada et al. 2015) for all sections from which u-channel samples were collected. CCSF-A depth scales were assigned to stacked image for Holes U1424A and U1424B so that stacked images could be directly compared with the u-channel paleomagnetic data. We extracted RGB values from the images at every 2 mm resolution and calculated mean RGB values for sediments from the same depth level. The acquired RGB values were then used to estimate L*, a*, and b* data following the calibration and formulae provided by Irino et al. (2018). The calculated L* values were then smoothed using 5-point moving average. The smoothed L* curve was subsequently interpolated at 1-cm intervals that match the same depth levels of the u-channel paleomagnetic data.

Tephra analyses

Chemical compositions of volcanic glass shards from sixteen selected depth intervals in Hole U1424A (see Table 1) were analyzed for major oxides on an energy dispersive spectroscopy (EDS) type electron probe micro-analyzer (EPMA) at the Fukushima University, Japan. Tephra samples were mounted in an epoxy resin on a slide glass. Sample surfaces were polished until glass shards were exposed. The samples then went through ultrasonic washing and drying process before they were carbon coated. Measurement conditions used are 15kV accelerating voltage, 0.5 nA electric current on a faraday cup, and a 5 µm × 5 µm beam scanning area. The obtained major element compositions were further calibrated by X-ray fluorescence (XRF) analytical results of the well characterized dacite to rhyolite representative volcanic glasses analyzed during the same analytical session (Nagahashi et al. 2003).

The correlation of each tephra was examined with ones at other sites and/or with other known tephras in terrestrial deposits characterized by their properties, litho-, bio-, magneto-stratigraphy and estimated ages. Tephrostratigraphy in the Pliocene to Holocene series on the Japanese Archipelago is based on widespread tephras (e.g. Machida 1999; Nagahashi et al. 2004; Satoguchi and Nagahashi 2012), with their characteristics described by both major and trace element compositions of volcanic glass shards (e.g. Kimura et al. 2015; Nagahashi et al. 2003, 2004, 2015).

Results and Discussion

Magnetic properties of the Site U1424 sediments

Representative results from rock magnetic experiments using the scraping samples are shown in Fig. 2. Raw hysteresis loops of the samples are dominated by positive slopes suggesting presence of significant amount of paramagnetic materials in the sediments. Slope corrected hysteresis loops (Fig. 2a) and estimated saturation fields by HystLab show that studied samples appear to be mostly saturated at applied fields of less than ~350-400 mT. Weight normalized saturation magnetization (Ms) of the samples (based on slope corrected loops) vary on orders of 10^{-4} to 10^{-2} Am^2/kg (Fig. 2a). Sample from Core-section U1424A-3H-4A (~23.5 m CCSF-A) that comprises predominantly dark colored sediments appears to have significantly lower Ms than other samples. Coercivity of remanence (Bcr) of the samples is generally low and ranges between ~30-60 mT (Fig. 2b). Hysteresis parameter ratios (i.e. Mr/Ms and Bcr/Bc) of the samples are shown on a Day et al. (1977) plot in Fig. 2c. Results from the samples fall into the "pseudo-single domain" (PSD) category in the area associated with magnetite particles with sizes of about a few microns to few tens of microns (Dunlop 2002), although many issues including magnetic mineralogy and magnetic particle mixtures could potentially complicate the interpretation of domain state based on a Day et al. plot (see Roberts et al., 2018).

IRM acquisition and gradient data of the studied bulk sediments are shown in Fig. 2d-e. Raw IRM acquisition data were fitted using smoothing splines (with a smoothing parameter of 0.995) to suppress noise in the measurement data. IRM gradient curves were normalized so that total area underneath each curve is equal to 1. Weight normalized saturation remanence of these samples is on the order of 10^{-3} Am^2/kg (Fig. 2d). Gradients of the IRM data plotted on logarithmic field scale (Fig. 2e) generally follow normal distributions with mean coercivity of ~50 mT, consistent with a generally low coercivity magnetic mineral such as (titano)magnetite being the primary remanence carrier. Some samples (e.g. those from ~3.8, ~7.1, ~23.5, and ~96.8 m CCSF-A) appear to have slightly higher mean coercivity (~65-70 mT), possibly due to finer magnetic particles in those samples. The IRM acquisition curves do not seem to have completely saturated at higher fields suggesting a small contribution from high coercivity magnetic phases (e.g., hematite). FORC diagrams of the two samples show generally low coercivity (mostly centered at ~20-30 mT on the Bc axis) component with vertical spread between ~±30-40 mT on the Bu axis), consistent with presence of a predominantly PSD (titano)magnetite phase in the sediments (Roberts et al. 2000, 2014).

The two samples used for low temperature magnetic experiments show similar behaviors during low temperature cycling of the SIRM acquired at room temperature (RT-SIRM), and warming of the SIRM acquired at low temperature (LT-SIRM) following zero-field cooling (ZFC). Cooling curves of the RT-SIRM (Fig. 3a) first undergo a gradual increase and then a large decrease between ~100-150 K. The warming curves of the RT-SIRM generally overlap with the cooling curves below ~100 K. Both samples show significant loss (~11%) in RT-SIRM after the cooling and warming cycles. Warming curves of the LT- SIRM (after ZFC) for both samples (Fig. 3b) show abrupt drop at ~120 K, characteristic for (titano)magnetite due to

Verwey transition around this temperature range. The abrupt changes at ~120 K is even more evident on the derivatives of the LT-SIRM warming curves (Fig. 3c).

Samples used for the hysteresis loops, backfield, and IRM acquisition experiments were taken from a large range of depth levels and cover all four lithologic subunits at Site U1424. Weight normalized Ms and IRM values of these samples vary significantly downcore, presumably due to varying concentration of ferrimagnetic materials. But similarity in the shape of the hysteresis loops, Bcr values, and mean coercivity from the IRM gradient curves indicates that the samples are likely dominated by a low coercivity magnetic mineral common in U1424 sediments with a small contribution of high coercivity magnetic minerals (e.g. hematite). Although samples used for the FORC and the low temperature experiments were taken mostly from the upper part of the sediment sequence, results from these samples suggest that (titano)magnetite is the dominant low coercivity magnetic remanence carrier in the sediments. These results are consistent with previous work done by Vigliotti (1997) on Brunhes aged sediments from ODP Site 794, which show that the sediments are dominated by magnetite-type minerals with small contribution made by canted-antiferromagnetic minerals (hematite) and iron sulphides (pyrrhotite and/or greigite). Vigliotti (1997) also noted that the dark- and light-colored sediments are mineralogically similar but are different in terms of magnetic mineral concentration and grain size. Lower concentration of (titano)magnetite in the dark-colored sediments at Site U1424 is probably related to reductive diagenesis during which (titano)magnetite dissolves and forms pyrite that is paramagnetic and does not carry remanence. This process is typically associated with euxinic conditions during glacial stages when the dark-colored sediments were deposited and is likely driven by sea level changes (Vigliotti 1997; Tada et al. 1999). Although our rock magnetic experiments could not directly suggest presence of large amount of remanence carrying iron sulphides (e.g. pyrrhotite and/or greigite), it is possible that U1424 sediments contain some amount of pyrrhotite and/or greigite as a result of the reductive diagenesis.

U-channel NRM data and their fidelity

Typical NRM demagnetization behaviors of samples from both normal and reversed polarity intervals at varying depths of Site U1424 are shown in Fig. 4. A stable single magnetization component can be clearly defined using NRM data after demagnetization with peak fields above ~20 mT. Majority of the NRM for all samples were removed after AF demagnetization with peak field of 100 mT. This observation is consistent with the results from the rock magnetic experiments that (titano)magnetite is the main remanence carrier in Site U1424 sediments. Component inclination and corrected declination data together with MAD and α_{95} values for all u-channel samples from Site U1424 calculated using PCA analysis and Fisher statistics on NRM data from 20-80 mT demagnetization steps are shown in Fig. 5. These data are compared with NRM intensity after 35 mT demagnetization (i.e. $\mathrm{NRM}_{35\mathrm{mT}}$ intensity) as well as photos and estimated L* of core sections from which the u-channels were taken. Paleomagnetic data from any disturbed intervals due to coring or sampling, or from tephra layers are shown in lighter color on Fig.5 and are not used for magnetostratigraphic interpretations. In addition, NRM measurements from intervals within the top and bottom 3 cm of each u-channel sample are subjected to convolution effect of the SRM's sensor response (see Oda and Xuan 2014; Xuan and Oda 2015) and are not shown on Fig. 5.

NRM$_{35mT}$ intensity of Site U1424 sediments ranges between 10^{-5} to 10^{-2} A/m with majority of the values on the order of 10^{-4} A/m. The highest intensity values occur in the top ~15 m CCSF-A of the sediment sequence and are mostly on the orders of 10^{-3} to 10^{-2} A/m. MAD values associated with the PCA analysis vary closely (correlation coefficient ~0.48) with α_{95} estimates from Fisher statistics (see Fig. 5) suggesting the two types of NRM data quality measure generally yield consistent results. MAD and α_{95} values change significantly down core and appear to follow opposite trend to the NRM intensity data. Lowest MAD values occur in the top ~15 m CCSF-A where NRM intensity is highest and are mostly a few degrees (mean ~3.6° and std. ~3.7°), suggesting very well-defined paleomagnetic components. MAD values for samples from below ~15 m CCSF-A are higher (mean ~18.4° and std. ~10.7°) and reach a few tens of degrees at intervals with low NRM intensities. Nevertheless, majority of these samples still yield reasonably well-defined directions that are suitable for magnetostratigraphic interpretations.

There appears to be a broad relation between sediment color and NRM intensity of the samples. Similarly, a broad relation seems to exist between sediment color and MAD and α_{95} values as MAD and α_{95} values show clear opposite trend to NRM intensity (Fig. 5). As an example, core image, estimated L*, and NRM$_{35mT}$ intensity of Core U1424B-6H is shown in Fig. 6. Dark-colored sediment intervals between ~45.8-46.4 and between ~47.4-47.6 m CCSF-A are apparently associated with lower NRM intensities (Fig. 6a). This is consistent with the rock magnetic experiment results which suggest that (titano)magnetite concentrations are lower in dark-colored sediments presumably due to reductive diagenesis.

To check if the alternation of dark and light layers might have debilitated the paleomagnetic signal (especially directional data) preserved in these sediments, we compared histograms of NRM intensity and directional data from both dark- (with L* values <25) and lighter-colored (with L* values >45) sediments at Site U1424. As alternation of dark and light layers mainly occurred in Unit I (see Fig. 5), the histograms mainly count data from the top ~70 m of the sediment sequence. NRM intensity from lighter-colored sediments show generally stronger NRM intensity than that from dark-colored sediments (Fig. 6b). Occasionally, there are dark-colored intervals that show high NRM intensity possibly due to enhanced growth of authigenic greigite at some dark-colored intervals. However, corrected declination (Fig. 6c) and inclination (Fig. 6d) data from dark- and light-colored sediments show very similar distributions. Corrected declinations from both types of sediments show peak distributions around 0° or 360° and around 180° that correspond to data from normal and reversed polarity intervals respectively. Inclination data from both types of sediments show peak distributions close to expected inclinations of ± 59.4° at the latitude of Site U1424 assuming a geocentric axial dipole (GAD) field model. Similarity in directional data distributions of the two types of sediments is clear for results from normal polarity and appears less strong for results from reversed polarity. Inclinations from reversed polarity intervals in both types of sediments show peak distributions around the expected GAD inclination but are more spread out (i.e. have larger standard deviation) than inclinations from normal polarity intervals. This "spread-out" could be caused by the generally weak NRM of the sediments (especially those from below ~15 m CCSF-A) combined with incompletely removed vertical drilling overprints at occasional intervals that induce more influences on results from reversed intervals. In addition, the “spread-out” in reversed inclinations distribution is more obvious in dark-colored sediments, possibly due to smaller signal-to-noise ratios related to generally weaker NRM intensity in dark-colored sediments. Nevertheless, these results suggest that although dark-colored sediments often show lower NRM intensity and Site U1424 sediments could have experienced varying degree of reductive diagenesis, the reductive diagenesis does not seem to have debilitated recording of paleomagnetic directions in the sediments. Both dark- and light-colored sediments appear to have recorded paleomagnetic directions that can be used for magnetostratigraphic interpretations.

Magnetostratigraphy

Inclination and corrected declination data in Fig. 5 show clear patterns that can be correlated to geomagnetic polarity time scale (e.g. GPTS2012 in Gradstein et al. 2012) of the last ~4.89 Myr. During normal and reversed intervals, inclination data vary closely around the expected GAD inclinations of 59.4° and -59.4° (dash-dotted lines in Fig. 5) while corrected declinations vary around 0° (or 360°) and 180°, respectively. We use the following criteria/methods to identify polarity reversals at Site U1424 based on the u-channel NRM data: (1) the reversals are accompanied by both a sign switch in inclinations and an ~180° transition in corrected declinations; (2) if reversals are recorded in overlapping intervals of the two holes, CCSF-A depths of the reversals should closely match each other; (3) center position of a reversal is estimated by reviewing NRM data from individual u-channel samples that recorded the reversal, and averaging the closest positions on either side of the reversal that clearly show normal or reversed magnetization components (difference between the two positions is halved and used as uncertainty for the center position of the reversal); and (4) data used to define the reversals are not from disturbed intervals. Information about identified polarity reversals are summarised in Table 2 including Hole-Core-Section ID, center position and uncertainty, and depth of the reversals in m CSF-A and m CCSF-A. Uncertainties of the reversal positions typically range between a few cm to a few tens of cm. Identified reversals are also shown in the rightmost panel on Fig. 5 with their corresponding GPTS ages labeled.

The majority of geomagnetic polarity reversals in the last ~4.89 Myr in the GPTS are clearly identified in the u-channel NRM data. These reversals are marked in bold in Table 2. The following six reversals were recorded in overlapping intervals of Holes U1424A and U1424B: onset of the Jaramillo subchron, onset and end of the Reunion subchron, end of the Mammoth subchron, the Gauss/Gilbert boundary, and end of the Cochiti subchron. CCSF-A depths at which these reversals were recorded in the two holes are remarkably consistent, typically within a few cm to just over 10 cm (see Table 2). The Cobb Mountain subchronozone, top of the Kaena subchronozone, and bottom of the Nunivak subchronozone are less well defined in the sediments (labeled in grey on the rightmost panel of Fig. 5). There are apparent transitions in inclinations and corrected declinations associated with these four reversals, but the boundaries are less well defined than other recorded reversals. Inclination and corrected declination data appear to be nosier during intervals with NRM_{35mT} intensity lower than ~10^{-4} A/m level (e.g. ~30, ~46, ~70-80, ~96, ~143-147 m CCSF-A). Inclination data during these intervals sometimes show shallower values or even occasional values in opposite directions but they still average around the expected GAD values and provide support for the interpreted magnetostratigraphy.

Correlation of Site U1424 polarity stratigraphy to GPTS is mostly straightforward for boundaries between the Brunhes, Matuyama, Gauss, and Gilbert Chrons, as well as for most of the subchrons (except Cobb Mountain and Kaena) within the Matuyama and Gauss Chrons. For the top ~100 m CCSF-A sediments at Site U1424, a preliminary polarity stratigraphy based on partially demagnetized (up to 30 mT peak field) u-channel NRM data was reported in Tada et al. (2018). Those results supersede that based on shipboard half-core section NRM data (Tada et al. 2015) but are updated here using u-channel NRM data with full demagnetization sequence (up to 100 mT peak field) for a total of ~167.6 m sediment sequence recovered at IODP Site U1424. Depth levels of the identified reversals in sediments from the top ~100 m CCSF-A from this study are very consistent with those reported in Tada et al. (2018) with differences typically around just a few cm. We tentatively revise the top of Kaena subchronozone to ~95.81 m CCSF-A.

Magnetostratigraphic interpretation for Site U1424 sediments below ~100 m CCSF-A (i.e. mostly in the Gilbert Chronozone) is less straightforward. Based on shipboard NRM data which are low resolution, only partially demagnetized, and nosier, the Cochiti subchronozone was placed around 140 m CCSF-A (see Tada et al. 2015). Our results do not appear to support this. The interval between ~115.67-149.1 m CCSF-A are apparently dominated by negative inclinations, and do not show clear evidence of a normal polarity zone (Fig. 5). Although inclinations around 131.6 m CCSF-A in Hole U1424A show a brief interval with positive inclinations, the overlapping interval in Hole U1424B however show stable negative inclinations with low MAD values. Similarly, an apparent brief positive inclination interval in Hole U1424B around 136 m CCSF-A is not replicated in overlapping intervals in Hole U1424A. This interval occurs in the top of a core (i.e. U1424B-15H) that is often prone to drilling induced disturbance. We interpret the Cochiti subchronozone to be between ~149.1-154.2 m CCSF-A at Site U1424. This interpretation is supported by the identification of the Znp-Ohta tephra at ~142.7 m CCSF-A (see section below). The Nunivak subchronozone is recorded between ~159.3-162.1 m CCSF-A with a clearly defined top but a less well-defined bottom. Site U1424 sediments appear to have recorded the top of the Sidufjall subchronozone at ~165.7 m CCSF-A. The bottom of the studied Site U1424 sediment sequence should be within the Sidufjall subchronozone and close to (but not reaching) the bottom of the Sidufjall subchronozone.

Tephra correlation

We correlate sixteen tephra layers identified at Site U1424 to known tephras on the Japanese archipelago based on their chemical compositions and stratigraphic positions (see Tables 1 and 3). Major element compositions of volcanic glass shards from the studied tephras in U1424A sediments are also compared with data from the corresponding known Japanese tephras in Fig. S1 to demonstrate the tephra correlations made. An earlier version of the tephra correlation was utilized by Tada et al. (2018) but detailed tephra properties supporting the correlation were not reported. Here, we demonstrate the tephra correlation based on the analyzed data and include two new correlations corresponding to the Yellow I and Yellow II/III tephras. Tephra correlations reported here were also checked by their petrographic properties. These correlations allow us to transfer depositional ages of the widespread known tephras to Site U1424. Ages for the known tephras were typically acquired through studies of formations on land using associated horizon of the marine isotope stage with radiometric ages, fission track age and biostratigraphic markers (see Table 3).

Identified tephra layers at Site U1424 and their estimated ages are also listed on the rightmost panel of Fig. 5. Estimated ages of these identified tephras at Site U1424 agree very well with the interpreted magnetostratigraphy. For example, the Hkd-Ku tephra with an estimated age of ~0.75 Ma (Suzuki et al. 2005) is identified at ~26.54 m CCSF-A, just above the identified Brunhes/Matuyama boundary. Similarly, the Ass-Tmd2 and Sr-Ity tephras with estimated ages of ~2.62 and ~3.55 Ma respectively were identified at ~83.29 and ~114.7 m CCSF-A, greatly supporting the interpreted Matuyama/Gauss and Gauss/Gilbert boundaries. In addition, identification of the Yamada I and Ss-Pnk tephras at Site U1424 with estimated ages of ~0.95 and ~1.053 Ma are consistent with the interpreted top of the Jaramillo subchronozone (with an estimated age of ~0.988 Ma). Identification of the Yellow I and Yellow II/III tephras at ~46.4 and ~44.38 m CCSF-A with their estimated age within MIS 35 (~1.2 Ma) is generally consistent with the interpreted Cobb Mountain subchronozone (although not well defined in the U1424 sediments). The Ak-Kd18 and Eb-Fukuda tephras identified at ~47.925 and ~57.9 m

CCSF-A with estimated age of ~1.45 and ~1.75 Ma respectively provide extra constraint for the interpreted top of the Olduvai subchronozone beneath them. The Znp-Ohta tephra with an estimated age of ~3.95 Ma is identified at ~142.7 m CCSF-A, supporting the interpretation that the Cochiti subchronozne should be below it. All identified tephras also agree with magnetic polarity chrons and subchrons recorded in sections on land (Niitsuma 1976; Hayashida and Yokoyama 1983; Nakayama and Yoshikawa 1990), and can be integrated with the magnetostratigraphy to add valuable age control points within the polarity chrons and subchrons.

Age model and sedimentation rates of Site U1424 sediments

Depth to age tie points based on magnetostratigraphy and tephrostratigraphy from this study are plotted in Fig. 7. For the last ~3 Myr, we compare our results with the depth-age tie points acquired based on tuning of gamma ray attenuation (GRA) density and natural gamma radiation (NGR) of Site U1424 sediments (Tada et al. 2018) to a global benthic oxygen isotope stack record (Lisiecki and Raymo 2005). The tuning is justified because GRA density of Site U1424 sediments reflects diatom contents which are higher during interglacial high-stands (see Tada et al. 2018). Age tie points from within the last ~3 Myr are very consistent with one another (upper panel in Fig. 7) and fall within the depth-age relation range defined by biostratigraphic markers of this interval (see Tada et al. 2015; Kamikuri et al. 2017). For the interval prior to ~3 Ma, the u-channel data based magnetostratigraphy agrees well with identification of the two tephras in this interval (i.e. Sr-Ity and Znp-Ohta). These depth-age tie points are again broadly in agreement with biostratigraphic marks available for this interval. In particular, the preliminary interpretation of Cochiti subchronozone based on shipboard data was in conflict with the Znp-Ohta tephra and a diatom event (i.e. the first occurance of *Neodenticula Koizumii*; see Tada et al. 2015). The revised position of the Cochiti subchronozone to ~149.1-154.2 m CCSF-A in this study largely resolved this issue. According to this age model, bottom of the Site U1424 sediment sequence covered by the u-channel samples at ~167.6 m CCSF-A is dated to ~4.89 Ma, assuming extrapolation of linear sedimentation rate between the bottom of the Nunivak and the top of the Sidufjall subchronozones.

Site U1424 sediment accumulation rates based on the magnetostratigraphy and tephrostratigraphy as well as the tuned chronology (last ~3 Myr only) are shown in lower panel of Fig. 7. Sedimentation rates range between ~1.7 to 7.6 cm/kyr with an average of ~3.3 cm/kyr. The highest mean sedimentation rate of ~7.6 cm/kyr occurred between ~3.6-3.95 Ma, while lowest mean sedimentation rates of ~1.7-2 cm/kyr happened at ~2, ~3, and prior to ~4.5 Ma. There appears to be an overall increasing trend in sedimentation rates since ~2 Ma. These changes in sedimentation rates likely reflect the amount and relative proportion of various source materials been transported and deposited at Site U1424, including fluvial sediments from the Japanese island rivers, eolian dust from central Asia, as well as materials from rivers in Russia, Korea, and China (see Irino and Tada 2002; Milliman and Farnsworth 2011; Shen et al. 2017). The highest mean sedimentation rate of ~7.6 cm/kyr between ~3.6-3.95 Ma occurred in the middle of Subunit IIB (Fig. 5). Shipboard GRA density data (Tada et al., 2015) show low values during this interval suggesting high diatom flux during this time period which could have contributed to the elevated sedimentation rates. The integrated magneto- and tephrostratigraphy provide a robust chronology at Site U1424 covering the last ~4.89 Ma. This chronology can be transferred to other sites drilled during IODP Expedition 346 through detailed correlation of dark and light layers as well as reversals and tephra layers, providing anchors to a "paleo-observatory network" (see Tada et al. 2018). In addition, Site U1424 could serve as a regional stratigraphic reference site to facilitate the study of other sediment sequences in the Japan Sea as well as Pliocene-Pleistocene formations on land (e.g. the Kazusa Group widely distributed in the central part of the Boso Peninsula; see Kazaoka et al. 2015) to investigate paleoceanographic and paleoenvironmental conditions in the region and their links to global changes.

Conclusions

Rock magnetic analyses on bulk samples from IODP Site U1424 indicate that magnetic remanence carriers in the sediments are primarily (titano)magnetite with small contribution of high coercivity magnetic minerals (e.g. hematite) and possibly iron sulphides (e.g. pyrrhotite and/or greigite). Concentration of (titano)magnetite appears significantly lower in dark-colored sediments, probably due to reductive diagenesis under euxinic conditions during which (titano)magnetite dissolves and forms pyrite that is paramagnetic. Comparison of histograms of NRM intensity and directional data from dark- and light-colored sediments suggest that although dark-colored sediments often show lower NRM intensity, both dark- and light-colored sediments have recorded paleomagnetic directional data that can be used to construct magnetostratigraphy.

Geomagnetic polarity boundaries between the Brunhes, Matuyama, Gauss, and Gilbert Chronozones are clearly recorded in Site U1424 sediments at ~27.54, ~81.3, and ~115.67 m CCSF-A respectively. In addition, the Jaramillo, Olduvai, and Reunion subchronozones within the Matuyama Chronozone are well preserved between ~34.92-37.56, ~59.69-63.91, and ~67.96-68.3 m CCSF-A. The Cobb Mountain subchronozone is less well defined. The apparent inclination switch accompanied by ~180° shift in declination suggests its possible recording between ~40.6-40.8 m CCSF-A. Within the Gauss Chronozone, the Mammoth subchronozone is clearly recorded between ~101.87-104.7 m CCSF-A. The bottom of the Kaena subchronozone appears well preserved at ~98.44 m CCSF-A, but the top of the Kaena subchronozone is less well defined and has been tentatively placed at ~95.81 m CCSF-A based on patterns in both declination and inclination data. The Cochiti and Nunivak subchronozones within Gilbert Chronozone are recorded at ~149.1-154.21 and ~154.21-162.1 m CCSF-A respectively, with bottom of the Nunivak subchronozone less well recognized. The Sidufjall subchronozone is partly recorded at Site U1424 with its top located at ~165.68 m CCSF-A.

We analysed and correlated sixteen tephra layers in Site U1424 sediments to reference tephrostratigraphy of the region. Ages of these identified tephras agree very well with the interpreted magnetostratigraphy, and can be integrated with the magnetostratigraphy to add valuable age control points within the recognized polarity chrons and subchrons. The integrated magneto- and tephrostratigraphy suggest that Site U1424 covered sediments deposited during the last ~4.89 Myr, with sediment accumulation rates range between ~1.7 to 7.6 cm/kyr with an average of ~3.3 cm/kyr. The robust age model obtained at Site U1424 makes it possible to use the site as a stratigraphic reference record for studies of Pliocene-Pleistocene marine and land sections in the region.

Abbreviations

AF: Alternating field; APC: Advanced piston corer; CCSF: Core composite depth below sea floor; CMCR: Center for Advanced Marine Core Research; CSF: Core depth below sea floor; EDS: Energy dispersive spectroscopy; EPMA: Electron probe micro-analyzer; FORC: First order reversal curve; GAD: geocentric axial dipole; GPTS: geomagnetic polarity time scale; GRA: Gamma ray attenuation; IODP: Integrated ocean drilling program; IRM: isothermal remanent magnetization; MAD: maximum angular deviation; NRM: Natural remanent magnetization; ODP: Ocean drilling program; PCA: Principal component analysis; PSD: pseudo-single domain; RGB: Red, green, blue; SIRM: saturation isothermal remanent magnetization; SRM: Superconducting rock magnetometer; TWC: Tsushima warm current; VSM: Vibrating sample magnetometer; XRF: X-ray fluorescence; ZFC: Zero field cooled.

Declarations

Availability of data and material

Please contact author for data requests.

Competing interests

The authors declare that they have no competing interest.

Funding

Paleomagnetism work in this study was supported by UK Natural Environment Research Council (NERC) grants NE/N004736/1 and NE/R011281/1 awarded to CX. Low temperature rock magnetic work was supported by Japan Society for the Promotion of Science (JSPS) KAKENHI grant JP17K14408 awarded to SS, and was performed under the cooperative research program of Center for Advanced Marine Core Research, Kochi University (Accept No.17A052, 17B052). Tephra analyses work was supported by the JSPS KAKENHI grant JP25400493 and JP21340144 awarded to YS and YN, respectively.

Authors' contributions

CX proposed the topic, designed the paleomagnetism and rock magnetism study, analyzed and interpreted the paleomagnetic and rock magnetic data, and wrote the manuscript. YJ carried out the paleomagnetic experiments on u-channel samples and room temperature rock magnetic experiments on bulk samples, analyzed the data, and contributed to the writing and editing of the manuscript. SS carried out the low temperature rock magnetic experiments, analysed the results, and contributed to the writing and editing of the manuscript. YS and YN conducted the tephra analyses, analyzed and interpreted tephra related data, and wrote tephra work related sections. All authors read and approved the manuscript.

Authors' information

CX is associate professor at University of Southampton; YJ is research technician at University of Southampton; SS is research scientist at National Institute of Advanced Industrial Science and Technology (AIST), Japan; YS is research scientist at Lake Biwa Museum; YN is professor at Fukushima University.

Acknowledgements

We thank the captain, crew, and shipboard scientists of IODP Expedition 346 for their contributions to the recovery and preliminary analysis of sediments used in this study. The authors are grateful to IODP Expedition 346 scientists and staff at Kochi Core Center for their assistance with the sampling and shipping of the u-channels. We thank two anonymous reviewers and the editor for their helpful comments and suggestions that improved the manuscript. We also thank Benjamin Griffin and Michael Egbulefu who conducted NRM measurement for some of the u-channel samples as part of their undergraduate dissertation work at the University of Southampton.

References

Aoki K, Irino T, Oba T. (2008) Late Pleistocene tephrostratigraphy of the sediment core MD01-2421 collected off the Kashima coast, Japan. The Quat Res (Daiyonki Kenkyu) 47:391-407. (in Japanese with English Abstract)

Dunlop DJ (2002) Theory and application of the Day plot (Mrs/Ms versus Hcr/Hc) 1. Theoretical curves and tests using titanomagnetite data. J Geophys Res-Solid Earth 107 (B3): 2056. doi:10.1029/2001jb000486

Egli R (2013) VARIFORC: An optimized protocol for calculating non-regular first-order reversal curve (FORC) diagrams. Glob Planet Change 110:302-320. doi:10.1016/j.gloplacha.2013.08.003

Expedition 346 Scientists (2014) Asian Monsoon: onset and evolution of millennial-scale variability of Asian monsoon and its possible relation with Himalaya and Tibetan Plateau uplift. IODP Prel Rept 346. doi:10.2204/iodp.pr.346.2014

Gradstein FM, Ogg JG, Schmitz M, Ogg G (2012) The Geologic Time Scale 2012: Amsterdam (Elsevier).

Hamano Y, Krumsiek KAO, Vigliotti L, Wippern JM (1992) Pliocene–Pleistocene magnetostratigraphy of sediment cores from the Japan Sea. In Tamaki K, Suyehiro K, Allan J, McWilliams M et al. Proc ODP Sci Results 127/128 (Pt. 2): College Station, TX (Ocean Drilling Program), 969–982. doi:10.2973/odp.proc.sr.127128-2.216.1992

Harrison RJ, Feinberg JM (2008) FORCinel: An improved algorithm for calculating first-order reversal curve distributions using locally weighted regression smoothing. Geochem Geophys Geosyst 9: Q05016. 10.1029/2008gc001987

Hayashida A, Yokoyama T (1983) Paleomagnetic chronology of the Plio-Pleistocene Kobiwako Group to the southeast of Lake Biwa, Central Japan. Jour Geol Soc Japan, 89:209-221.

Heslop D, Roberts AP (2012) Estimation of significance levels and confidence intervals for first-order reversal curve distributions. Geochem Geophys Geosyst 13:Q12Z40. https://doi.org/10.1029/2012GC004115

Ingle, JC, Suyehiro K, von Breymann, MT et al. (1990) Proc ODP Init Repts 128: College Station, TX (Ocean Drilling Program). doi:10.2973/odp.proc.ir.128.1990

Irino T, Tada R, Ikehara K, Sagawa T, Karasuda A, Kurokawa S, Seki A, Lu S (2018) Construction of perfectly continuous records of physical properties for dark-light sediment sequences collected from the Japan Sea during Integrated Ocean Drilling Program Expedition 346 and their potential utilities as paleoceanographic studies. Prog Earth Planet Sc 5: 23. https://doi.org/10.1186/s40645-018-0176-7

Irino T, Tada R, (2002) High-resolution reconstruction of variation in aeolian dust (Kosa) deposition at ODP site 797, the Japan Sea, during the last 200 ka. Glob Planet Change 35:143–156.

Jackson M, Solheid P (2010) On the quantitative analysis and evaluation of magnetic hysteresis data. Geochem Geophys Geosyst 11(4): Q04Z15. doi:10.1029/2009gc002932

Kamikuri S-I, Itaki T, Motoyama I, Matsuzaki KM (2017) Radiolarian Biostratigraphy from Middle Miocene to Late Pleistocene in the Japan Sea. Paleontological Research 21 (4):397-421.

Kazaoka O, Suganuma Y, Okada M, Kameo K, Head MJ, Yoshida T, Sugaya M, Kameyama S, Ogitsu I, Nirei H, Aida N, Kumai H (2015) Stratigraphy of the Kazusa Group, Chiba Peninsula, Central Japan: an expanded and highly-resolved marine sedimentary record from the Lower and Middle Pleistocene. Quat Int 383:116–134.

Kimura J, Nagahashi Y, Satoguchi Y, Chang Q (2015) Origins of felsic magmas in Japanese subduction zone: Geochemical characterizations of tephra from caldera-forming eruptions <5 Ma. Geochem Geophys Geosyst 16:2147-2174.

Kirschvink JL (1980) The least-squares line and plane and the analysis of paleomagnetic data. Geophys J InT 62(3):699-718.

Kurokawa K, Nagahashi Y, Yoshikawa S, Satoguchi Y (2008) Correlation of the Asashiro Tephra Bed in the Osaka Group and the Tzw Tephra Bed in the Niigata region in central Japan. The Quat Res, 47:93-99. (Japanese with English abstract)

Lisiecki LE, Raymo ME (2005) A Pliocene-Pleistocene stack of 57 globally distributed benthic δ^{18}O records. Paleoceanography 20(1):PA1003. doi:10.1029/2004PA001071

Machida H (1999) The stratigraphy, chronology and distribution of distal marker-tephras in and around Japan. Global Planet Change 21:71-94.

Milliman JD, Farnsworth KL (2011) River Discharge to the Coastal Ocean: A Global Synthesis. Cambridge Univ Press.

Nagahashi Y, Nakai S, Kikkawa K, Okudaira T, Yoshikawa S and Yoshida T (2015) Petrological properties of tephra beds based on the major and trace element composition of volcanic glass shards - a case study of the Osaka Group and the Takashima-oki drilling core sediments in Lake Biwa, Kinki district, Japan. Earth Science (Chikyu Kagaku) 69: 205-222. (in Japanese with English Abstract)

Nagahashi Y, Yoshida T, Nakai S, Okudaira T (2003) Evaluation and correction of EDS Results of the glass shards from some representative tephra by comparison with XRF Analysis. The Quat Res (Daiyonki Kenkyu) 42:265-277. (in Japanese with English Abstract)

Nagahashi Y, Yoshikawa S, Miyakawa C, Uchiyama T and Inouchi Y (2004) Stratigraphy and chronology of widespread tephra layers during the Past 430ky in the Kinki District and the Yatsugatake Mountains: major element composition of the glass shards using EDS analysis. The Quat Res (Daiyonki-kenkyu) 43:15-35. (in Japanese with English Abstract)

Nakayama K, Yoshikawa Y (1990) Magnetostratigraphy of the late Cenozoic Tokai Group in central Japan. Jour Geol Soc Japan 96:967-976. (in Japanese with English Abstract)

Niitsuma N (1976) Magnetic stratigraphy in the Boso Peninsula. Jour Geol Soc Japan 82:163-181. (in Japanese with English abstract)

Nozaki A, Majima R, Kameo K, Sakai S, Kouda A, Kawagata S, Wada H, Kitazato H (2014) Geology and age model of the Lower Pleistocene Nojima, Ofuna, and Koshiba Formations of the middle Kazusa Group, a forearc basin-fill sequence on the Miura Peninsula, the Pacific side of central Japan. Island Arc, 23:157-179.

Oba T, Kato M, Kitazato H, Koizumi I, Omura A, Sakai T, Takayama T (1991) Paleoenvironmental changes in the Japan Sea during the last 85,000 years. Paleoceanography 6(4):499-518

Oda H, Xuan C (2014) Deconvolution of continuous paleomagnetic data from pass-through magnetometer: A new algorithm to restore geomagnetic and environmental information based on realistic optimization. Geochem Geophys Geosyst 15:3907-3924. https://doi.org/10.1002/2014GC005513

Paterson GA, Zhao X, Jackson M, Heslop D (2018) Measuring, Processing, and Analyzing Hysteresis Data. Geochem Geophys Geosyst 19(7):1925-1945. doi:10.1029/2018gc007620

Pickering KT, Couter C, Oba T, Taira A, Schaaf M, Platzman E (1999) Glacio-eustatc control on deep-marine clastic forearc sedimentation, Pliocene-mid-Pleistocene (c. 1180-600 ka) Kazusa Group, SE Japan. Jour Geol Soc London, 156: 125-136.

Pike CR, Roberts AP, Verosub KL (1999) Characterizing interactions in fine magnetic particle systems using first order reversal curves. J Appl Phys 85 (9):6660-6667

Roberts AP, Heslop D, Zhao X, Pike CR (2014) Understanding fine magnetic particle systems through use of first-order reversal curve diagrams. Rev Geophys 52(4):557-602. doi:10.1002/2014rg000462

Roberts AP, Pike CR, Verosub KL (2000) First-order reversal curve diagrams: A new tool for characterizing the magnetic properties of natural samples. J Geophys Res 105(B12):28461-28475. doi:Doi 10.1029/2000jb900326

Roberts AP, Tauxe L, Heslop D, Zhao X, and Jiang Z (2018) A Critical Appraisal of the “Day” Diagram: J Geophys Res 123. doi:10.1002/2017JB015247

Satoguchi Y, Higuchi Y, Kurokawa K (2005) Correlation of the Ohta Tephra Bed in the Tokai Group with a tephra bed in the Miura Group, central Japan. Jour Geol Soc Japan 111: 74-86. (in Japanese with English Abstract)

Satoguchi Y, Nagahashi Y (2012) Tephrostratigraphy of the Pliocene to Middle Pleistocene Series in Honshu and Kyushu Islands, Japan. Island Arc 21: 149-169.

Shen XY, Wan SM, France-Lanord C, Clift PD, Tada R, Revillon S, Shi XF, Zhao DB, Liu YG, Yin XB, Song ZH, Li AC (2017) History of Asian eolian input to the Sea of Japan since 15 Ma: Links to Tibetan uplift or global cooling? Earth Planet Sci Lett 474:296-308. doi:10.1016/j.epsl.2017.06.053

Shirai M, Tada R, Fujioka K (1997) Identification and chronostratigraphy of middle to upper Quaternary marker tephras occurring in the Anden coast based on comparison with ODP cores in the sea of Japan. Quat Res (Daiyonki-Kenkyu) 36:183–196 (in Japanese with English abstract)

Smith VC, Staff RA, Blockley SPE,Ramsey CB, Nakagawa T, Mark DF, Takemura K, Danhara T, Suigetsu 2006 Project Members (2013) Identification and correlation of visible tephras in the Lake Suigetsu SG06 sedimentary archive, Japan: chronostratigraphic markers for synchronising of east Asian/west Pacific palaeoclimatic records across the last 150 ka. Quat Sci Rev 67:121-137.

Suzuki T, Eden D, Danhara T, Fujiwara O (2005) Correlation of the Hakkoda-Kokumoto Tephra, a widespread Middle Pleistocene tephra erupted from the Hakkoda Caldera, northeast Japan. Island Arc 14: 666-678.

Tada R (1994) Paleoceanographic evolution of the Japan Sea. Palaeogeography, Palaeoclimatology, Palaeoecology 108(3):487-508.

Tada R (2005) Onset and evolution of millennial-scale variability in the Asian Monsoon and its impact on paleoceanography of the Japan Sea. Millennial-Scale Variability in the Asian Monsoon, American Geological Union, U.S.A, pp 1–16

Tada R (2012) The Japan Sea sediments and variability of East Asian Monsoon: toward the IODP drilling of the Japan Sea and East China Sea. Quat Res (Tokyo) 51(3):151–164

Tada R, Irino T, Ikehara K, Karasuda A, Sugisaki S, Xuan C, Sagawa T, Itaki T, Kubota Y, Lu S, Seki A, Murray RW, Alvarez-Zarikian C, Anderson WT, Bassetti MA, Brace BJ, Clemens SC, Gurgel MHD, Dickens GR, Dunlea AG, Gallagher SJ, Giosan L, Henderson ACG, Holbourn AE, Kinsley CW, Lee GS, Lee KE, Lofi J, Lopes CICD, Saavedra-Pellitero M, Peterson LC, Singh RK, Toucanne S, Wan SM, Zheng HB, Ziegler M (2018) High-resolution and high-precision correlation of dark and light layers in the Quaternary hemipelagic sediments of the Japan Sea recovered during IODP Expedition 346. Prog Earth Planet Sc 5:19. doi:10.1186/s40645-018-0167-8

Tada R, Irino T, Koizumi I (1999) Land-ocean linkages over orbital and millennial timescales recorded in late Quaternary sediments of the Japan Sea. Paleoceanography 14(2):236-247. doi:10.1029/1998pa900016

Tada R, Koizumi I, Cramp A, Rahman A (1992) Correlation of dark and light layers, and the origin of their cyclicity in the Quaternary sediments from the Japan Sea. In Pisciotto, K. A., Ingle, J. C, Jr., von Breymann, M. T., Barron, J., et al. Proc ODP, Sci results, 127/128, Pt. 1: 577–601 College Station(Ocean Drilling Program)

Tada R, Murray RW, Alvarez Zarikian CA, Anderson WT, Jr., Bassetti MA, Brace BJ, Clemens SC, da Costa Gurgel MH, Dickens GR, Dunlea AG, Gallagher SJ, Giosan L, Henderson ACG, Holbourn AE, Ikehara K, Irino T, Itaki T, Karasuda A, Kinsley CW, Kubota Y, Lee GS, Lee KE, Lofi J, Lopes CICD, Peterson LC, Saavedra-Pellitero M, Sagawa T, Singh RK, Sugisaki S, Toucanne S, Wan S, Xuan C, Zheng H, Ziegler M (2015) Site U1424. In. Proc IODP. doi:10.2204/iodp.proc.346.105.2015

Tada R, Murray RW, Zarikian CAA (2013) Asian Monsoon: onset and evolution of millennial-scale variability of Asian Monsoon and its possible relation with Himalaya and Tibetan plateau uplift. IODP Sci. Prosp. 346. doi:10.2204/iodp.sp.346.2013

Tamaki K, Pisciotto K, Allan J et al. (1990) Proc. ODP, Init Repts 127: College Station, TX (Ocean Drilling Program). doi:10.2973/odp.proc.ir.127.1990

Tauxe L, Labrecque J, Dodso D, Fuller M (1983) "U" channels - a new technique for paleomagnetic analysis of hydraulic piston cores. EOS Trans AGU 64:219.

Tsuji T, Miyata Y, Okada M, Mita I, Nakagawa H, Sato Y, Nakamizu M (2005) High-resolution chronology of the lower Pleistocene Otadai and Umegase Formations of the Kazusa Group, Boso Peninsula, central Japan –Chronostratigraphy of the JNOC TR-3 cores based of oxygen isotope, magnetostratigraphy and calcareous nannofossil. Jour Geol Soc Japan 111: 1-20. (in Japanese with English Abstract)

van Peer TE, Xuan C, Lippert PC, Liebrand D, Agnini C, Wilson PA (2017) Extracting a Detailed Magnetostratigraphy From Weakly Magnetized, Oligocene to Early Miocene Sediment Drifts Recovered at IODP Site U1406 (Newfoundland Margin, Northwest Atlantic Ocean). Geochem Geophys Geosyst 18. doi:10.1002/2017gc007185

Vigliotti L (1997) Magnetic properties of light and dark sediment layers from the japan sea: Diagenetic and paleoclimatic implications. Quat Sci Rev 16(10):1093-1114. https://doi.org/10.1016/S0277-3791(96)00118-7

Watanabe M (2002) Revised diatom biostratigraphy and chronostratigraphy of the Pliocene sequence in Himi-Nadaura area, Toyama Prefecture, central Japan: With special reference to ages of widespread volcanic ash beds and No.3 Globorotaliia inflata bed of planktonic foraminiferal biostratigraphy. Jour Geol Soc Japan 108: 499-509. (in Japanese with English abstract)

Xuan C, Channell JET (2009) UPmag: MATLAB software for viewing and processing u channel or other pass-through paleomagnetic data. Geochem Geophys Geosyst 10:Q10Y07. doi:10.1029/2009gc002584

Xuan C, Oda H (2019) Sensor Response Estimate and Cross Calibration of Paleomagnetic Measurements on Pass-Through Superconducting Rock Magnetometers. Geochem Geophys Geosyst 20. https://doi. org/10.1029/2019GC008597

Xuan C, Oda H (2015) UDECON: deconvolution optimization software for restoring high-resolution records from pass-through paleomagnetic measurements. Earth Planets Space 67: 183. https://doi.org/10.1186/s40623-015-0332-x

Yoshikawa S, Mitamura, M (1999) Quaternary stratigraphy of the Osaka Plain, central Japan and its correlation with oxygen isotope record from deep sea cores. Jour Geol Soc Japan 105: 332-340. (in Japanese with English Abstract)

Figure Legends

Figure 1. Location of Site U1424 and other sites drilled during IODP Expedition 346. Arrows indicate flow directions of surface currents. TWC: Tsushima warm current.

Figure 2. Room temperature rock magnetic analyses results of selected bulk sediment samples from Site U1424. Measurements were conducted on a vibrating sample magnetometer (VSM). (a) Slope corrected hysteresis loops; (b) IRM backfield curves; (c) hysteresis parameters plotted on a Day et al. (1977) plot; (d) IRM acquisition data; (e) gradient of IRM acquisition; and (f-g) FORC diagrams. Hysteresis loops, IRM backfield experiment, and IRM acquisition data are weight normalized. Gradient of IRM curves are normalized so that total area underneath each curve is equal to 1. Color of data curves and points in (b) and (c) share the same key shown in (a), and data curves in (e) share the same key shown in (d). Depth of samples listed is in m CCSF-A.

Figure 3. Low temperature rock magnetic experiment results of two samples from Site U1424. (a) Saturation isothermal remanent magnetization acquired at room temperature (RT-SIRM) monitored on cooling from 300 K to 10 K and subsequent warming back to 300 K; (b) SIRM acquired at low temperature (LT-SIRM) after zero-field cooling monitored on warming; and (c) derivative of the LT-SIRM warming curves. Note that RT-SIRM and LT-SIRM curves have been normalized to SIRM of samples at 300 K and at 10 K respectively. The derivatives of LT-SIRM were calculated based on a smoothed version of the raw data to avoid influence from occasional noisy measurements. Depth of samples listed is in m CCSF-A.

Figure 4. Representative orthogonal projections of NRM demagnetization data. Examples shown include results from selected 1-cm intervals in different polarity zones recorded by Site U1424 sediment sequence. Circles (red) and squares (blue) indicate projections onto vertical and horizontal planes, respectively (unit for axes are × 10^{-3} A/m). The 20 mT and 80 mT demagnetization steps are labeled. Hole-core-section and position (in cm) and depth (in m CCSF-A) information associated with each 1-cm interval data is also labeled.

Figure 5. Down-core changes in Site U1424 sediment color and NRM data with interpreted magnetostratigraphy and tephrostratigraphy. From left to right: image of core-sections used in this study, lithologic units and subunits, L* estimated from core images, NRM intensity data (35 mT demagnetization step), MAD values (blue) and α_{95} (purple) associated with the PCA

analyses and Fisher mean calculations, corrected PCA (green) and Fisher mean (gray) declinations, PCA (red) and Fisher mean (gray) inclinations, and interpreted magnetic polarity stratigraphy (black and white bars) and tephrochronology (horizontal red bars and labels). Core names (e.g. A1, B2) and section breaks are marked next to the core-section images. Light and dark gray points on L* plot are values estimated at 2-mm and 1-cm intervals respectively. Vertical gray dash-dotted lines on the inclination plot are expected inclinations during reversed and normal polarity intervals at Site U1424 assuming a geocentric axial dipole (GAD) field. NRM data, MAD and α_{95} values from disturbed and tephra intervals are shown in lighter color, and not used for magnetostratigraphy interpretations.

Figure 6. Comparison of NRM intensity and directional data from dark- and light-colored sediments at Site U1424. (a) Comparison of core-section photo, L*, and NRM_{35mT} intensity data from an example interval in Core U1424B-6H; and histograms of (b) NRM_{35mT} intensity, (c) mean corrected declination, and (d) mean inclination data from dark- (blue bars) and light-colored (orange bars) sediments. Dark- and light- colored sediments are set to intervals with L* values <25 and >45, respectively. Data from disturbed intervals are not included in the histograms. Light and dark gray points in (a) are L* values estimated using the core-section photos at 2-mm and 1-cm intervals, respectively. Vertical green dashed lines on (d) are expected inclinations during reversed and normal polarity intervals at Site U1424 assuming a GAD field.

Figure 7. Age model and sedimentation rates of Site U1424 sediments. Top panel: depth-age model of Site U1424 sediments between 0-167.6 m CCSF-A (~0-4.89 Ma) based on polarity reversals (black squares), tephra (red triangles) chronology, and tuning of U1424 GRA and NGR data to a global benthic oxygen isotope stack (green dots; see Tada et al. 2018). Bottom panel: Site U1424 sedimentation rate changes through time estimated using tuned ages for the last ~3 Myr and magnetostratigraphy and tephra ages for intervals older than ~3 Ma.

Supplementary Figure Legend

Figure S1. Major element compositions of volcanic glass shards from studied tephras in U1424A sediments compared with data from correlated known Japanese widespread tephras. FeO* is the total iron recalculated as FeO. The pale bars indicate the standard deviations.

Table 1. Major element composition of tephra samples from Hole U1424A based on EDS analysis.

Sample ID	Core - Section	Offset (cm)	CCSF-A (m)		Major element composition by EDS analysis (mean wt.%)									n =	Total (raw)	Correlative tephra
					SiO_2	TiO_2	Al_2O_3	FeO*	MnO	MgO	CaO	Na_2O	K_2O			
NK 371	1-1	135.5	1.355	Av	76.78	0.19	13.12	1.30	0.02	0.12	1.05	3.55	3.87	11	94.33	AT
				sd	0.77	0.10	0.34	0.42	0.04	0.08	0.21	0.15	0.55		0.94	
NK 373	1-3	98.0	3.980	Av	71.34	0.48	15.31	1.78	0.11	0.44	1.30	4.65	4.59	12	95.74	Aso-4
				sd	0.75	0.09	0.28	0.27	0.11	0.09	0.20	0.16	0.20		1.18	
NK 375	1-4	26.0	4.760	Av	77.57	0.08	13.16	0.92	0.06	0.06	0.45	4.60	3.09	12	94.84	Toya
				sd	0.49	0.07	0.28	0.11	0.07	0.05	0.06	0.24	0.10		0.70	
NK 380	2-6	117.0	16.240	Av	65.13	0.34	16.66	4.54	0.13	0.24	1.20	6.09	5.67	15	94.00	B-Og
				sd	0.58	0.11	0.17	0.32	0.09	0.07	0.13	0.20	0.18		1.77	
NK 387	3-5	27.0	24.470	Av	77.70	0.26	12.52	1.39	0.07	0.26	1.60	3.73	2.48	12	93.77	Ka1
				sd	0.24	0.08	0.16	0.20	0.07	0.08	0.09	0.17	0.10		0.76	
NK 391	3-6	84.0	26.540	Av	77.59	0.31	12.45	1.45	0.10	0.23	1.40	4.07	2.40	12	94.93	Hkd-Ku
				sd	0.42	0.10	0.19	0.15	0.09	0.06	0.13	0.18	0.12		0.84	
NK 397	4-4	28.0	33.880	Av	76.94	0.37	12.40	2.00	0.02	0.36	1.80	3.59	2.51	12	92.68	Yamada 1
				sd	0.28	0.11	0.15	0.15	0.04	0.09	0.07	0.12	0.06		0.62	
NK 404	4-6	19.0	36.790	Av	77.09	0.28	12.62	1.02	0.06	0.22	1.14	3.22	4.34	12	94.24	Ss-Pnk
				sd	0.34	0.08	0.15	0.11	0.08	0.06	0.11	0.19	0.15		0.54	
NK 413	5-4	58.0	44.380	Av	76.40	0.13	13.88	0.92	0.07	0.32	1.39	4.02	2.87	12	93.08	Yellow II or III
				sd	0.27	0.06	0.13	0.15	0.10	0.07	0.08	0.13	0.10		0.57	
NK 416	5-5	110.0	46.400	Av	77.27	0.18	13.07	0.91	0.10	0.19	1.08	3.59	3.61	12	93.31	Yellow I
				sd	0.15	0.08	0.14	0.15	0.10	0.06	0.05	0.07	0.11		0.69	
NK 418	5-6	112.5	47.925	Av	77.37	0.32	12.44	1.59	0.07	0.35	1.69	3.40	2.76	12	93.87	Ak-Kd18?
				sd	0.82	0.09	0.34	0.20	0.10	0.10	0.09	0.19	0.18		1.22	
NK 424	6-6	103.5	57.905	Av	75.57	0.14	13.39	1.61	0.05	0.13	1.04	3.76	4.31	12	93.47	Eb-Fukuda
				sd	0.26	0.08	0.18	0.22	0.07	0.07	0.08	0.19	0.12		0.54	
NK 431	8-5	32.0	74.740	Av	74.98	0.15	13.71	1.67	0.05	0.11	1.06	3.98	4.29	13	94.35	Msn-Jwg4
				sd	1.07	0.09	0.47	0.45	0.07	0.06	0.36	0.32	0.72		1.14	
NK 439	9-4	15.0	83.290	Av	75.10	0.33	13.60	1.52	0.11	0.29	1.42	3.97	3.66	12	93.94	Ass-Tmd2
				sd	0.31	0.10	0.13	0.18	0.10	0.06	0.11	0.12	0.18		0.58	
NK 139	12-5	79.0	114.670	Av	76.02	0.10	13.35	1.16	0.05	0.09	0.71	3.41	5.15	12	95.11	Sr-Ity
				sd	0.20	0.10	0.07	0.16	0.05	0.06	0.07	0.14	0.18		0.97	
NK 142	15-6	63.0	142.670	Av	76.38	0.06	13.52	0.93	0.08	0.11	0.65	3.26	5.07	12	94.27	Znp-Ohta
				sd	0.24	0.07	0.15	0.16	0.08	0.05	0.08	0.13	0.11		0.44	

FeO*: total iron recalculated as FeO, Av = average, sd = standard deviation.

Table 2. Polarity boundaries identified in collected u-channel samples from Holes U1424A and U1424B.

Polarity Boundaries	Age (Ma)	Hole-Core-Section	Centre position (cm)	Uncertainty (cm)	Depth CSF-A (m)	Depth CCSF-A (m)
(B) C1n (Brunhes/Matuyama)	0.781	**B-4H-2**	**112**	**±5**	24.32	27.54
(T) C1r.1n (Jaramillo)	0.988	**A-4H-4**	**132**	**±8**	31.62	34.92
(B) C1r.1n (Jaramillo)	1.072	**A-4H-6**	**96**	**±19**	34.26	37.56
		B-5H-3	52	±18	34.18	37.58
(T) C1r.2n (Cobb Mountain)	1.173	B-5H-5	54	±5	37.20	40.60
(B) C1r.2n (Cobb Mountain)	1.185	B-5H-5	76	±5	37.42	40.82
(T) C2n (Olduvai)	1.778	**B-7H-3**	**126**	**±5**	54.46	59.69
(B) C2n (Olduvai)	1.945	**B-7H-6**	**98**	**±5**	58.68	63.91
(T) C2r.1n (Reunion)	2.128	**A-7H-6**	**103**	**±7**	62.83	67.96
		B-8H-2	67	±10	61.87	67.93
(B) C2r.1n (Reunion)	2.148	**A-7H-6**	**137**	**±7**	63.17	68.30
		B-8H-2	**118**	**±10**	62.38	68.44
(T) C2An.1n (Matuyama/Gauss)	2.581	**B-9H-4**	**100**	**±12**	74.66	81.30
(T) C2An.1r (Kaena)	3.032	A-10H-5	115	±15	89.95	95.81
(B) C2An.1r (Kaena)	3.116	B-11H-2	110	±10	90.80	98.44
(T) C2An.2r (Mammoth)	3.207	**A-11H-3**	**67**	**±20**	95.35	101.87
		B-11H-5	**7**	**±5**	94.27	101.91
(B) C2An.2r (Mammoth)	3.33	**A-11H-5**	**50**	**±25**	98.18	104.70
(T) C2Ar (Gauss/Gilbert)	3.596	**A-12H-6**	**26**	**±5**	109.62	115.67
		B-13H-2	8	±5	107.51	115.64
(T) C3n.1n (Cochiti)	4.187	**A-16H-1**	**110**	**±5**	140.90	149.06
		B-16H-5	**45**	**±15**	142.15	149.10
(B) C3n.1n (Cochiti)	4.3	**A-16H-5**	**33**	**±20**	146.05	154.21
(T) C3n.2n (Nunivak)	4.493	**B-17H-5**	**55**	**±10**	151.75	159.34
(B) C3n.2n (Nunivak)	4.631	A-17H-3	92	±25	153.22	162.10
(T) C3n.3n (Sidufjall)	4.799	A-17H-5	150	±20	156.80	165.68

(B) = bottom; (T) = top. In bold are polarity boundaries that are defined with more confidence. Reversal ages are based on GPTS2012 (Gradstein et al. 2012).

Table 3. Summary of chemical composition of known tephras on the Japanese archipelago from the literature and this study.

Tephra name			Chemical composition (wt. %)									n =	Age (Reference)
(*reference)			SiO_2	TiO_2	Al_2O_3	FeO*	MnO	MgO	CaO	Na_2O	K_2O		
A-Tn	*2	Av	77.49	0.16	12.81	1.32	0.06	0.12	1.20	3.41	3.43	16	~30 ka (Smith et al. 2013)
		sd	0.32	0.08	0.09	0.17	0.07	0.08	0.09	0.15	0.09		
Aso-4	*2	Av	71.70	0.41	15.44	1.67	0.10	0.41	1.27	4.47	4.52	16	~87 ka (Aoki et al. 2008)
		sd	0.60	0.07	0.33	0.17	0.08	0.10	0.24	0.11	0.16		
Toya	*1	Av	77.72	0.09	13.25	1.04	0.08	0.11	0.31	4.38	3.02	30	~106 ka (Shirai et al. 1997)
		sd	0.30	0.08	0.21	0.12	0.11	0.06	0.09	0.20	0.23		
B-Og	*1	Av	65.00	0.39	16.80	4.71	0.15	0.23	1.11	6.00	5.61	35	~448 ka (Shirai et al. 1997)
		sd	0.53	0.15	0.17	0.28	0.12	0.11	0.12	0.17	0.14		
Ka1	**	Av	77.63	0.21	12.53	1.50	0.06	0.27	1.67	3.69	2.44	10	MIS 17, ~700 ka (Pickering et al. 1999)
		sd	0.25	0.08	0.17	0.19	0.06	0.08	0.07	0.12	0.11		
Hkd-Ku	*3	Av	77.20	0.27	12.45	1.55	0.08	0.28	1.43	4.32	2.43	15	MIS 19.1-18.4, ~750 ka (Suzuki et al. 2005)
		sd	0.45	0.08	0.22	0.08	0.11	0.08	0.10	0.12	0.07		
Yamada I	*3	Av	76.70	0.39	12.31	2.00	0.03	0.31	1.98	3.74	2.55	15	~950 ka (Yoshikawa and Mitamura 1999)
		sd	0.30	0.05	0.14	0.10	0.03	0.09	0.08	0.16	0.10		
Ss-Pnk	*3	Av	76.63	0.26	12.77	1.17	0.08	0.23	1.11	3.43	4.33	15	~1.053 Ma (Tsuji et al. 2005)
		sd	0.23	0.09	0.09	0.07	0.08	0.09	0.07	0.16	0.14		
Yellow III	*3	Av	76.05	0.20	13.68	1.07	0.07	0.32	1.44	3.94	3.22	15	MIS 35 (Yoshikawa and Mitamura 1999)
		sd	0.45	0.10	0.29	0.20	0.07	0.12	0.17	0.33	0.45		
Yellow II	*3	Av	76.14	0.15	13.77	1.06	0.03	0.31	1.49	3.94	3.12	15	MIS 35 (Yoshikawa and Mitamura 1999)
		sd	0.38	0.08	0.15	0.07	0.03	0.09	0.05	0.22	0.26		
Yellow I	*3	Av	76.93	0.21	13.05	0.95	0.06	0.24	1.02	3.72	3.81	15	MIS 35 (Yoshikawa and Mitamura 1999)
		sd	0.36	0.09	0.18	0.09	0.07	0.11	0.08	0.28	0.32		
Ak-Kd18	**	Av	77.66	0.33	12.35	1.57	0.06	0.31	1.68	3.34	2.74	11	~1.45 Ma (Satoguchi and Nagahashi 2012)
		sd	0.45	0.16	0.26	0.21	0.07	0.06	0.10	0.11	0.11		
Eb-Fukuda	*3	Av	75.48	0.10	13.42	1.62	0.05	0.11	0.99	3.87	4.35	15	MIS 62, ~1.75 Ma (Nozaki et al. 2014)
		sd	0.22	0.07	0.11	0.11	0.05	0.10	0.06	0.15	0.13		
Msn-Jwg4	**	Av	74.40	0.13	13.91	1.86	0.02	0.10	1.08	3.90	4.59	12	~2.3 Ma (Satoguchi and Nagahashi 2012)
		sd	0.21	0.09	0.25	0.20	0.05	0.09	0.10	0.16	0.28		
Ass-Tmd2	*3	Av	75.15	0.33	13.56	1.46	0.09	0.28	1.41	4.06	3.66	15	~2.62 Ma (Kurokawa et al. 2008)
		sd	0.47	0.10	0.16	0.15	0.11	0.09	0.10	0.17	0.12		
Sr-Ity	*3	Av	75.97	0.08	13.46	1.18	0.05	0.10	0.61	3.58	4.96	15	~3.55 Ma (Watanabe 2002)
		sd	0.26	0.07	0.10	0.13	0.07	0.06	0.08	0.15	0.13		
Znp-Ohta	**	Av	76.28	0.07	13.50	0.98	0.09	0.08	0.65	3.35	5.00	15	~3.95 Ma (Satoguchi et al. 2005)
		sd	0.21	0.12	0.18	0.22	0.15	0.08	0.09	0.18	0.27		

*1: Nagahashi et al. (2003), *2: Nagahashi et al. (2004), *3: Nagahashi et al. (2015), **: This study. FeO*: total iron recalculated as FeO, Av: average, sd: standard deviation.

Figure 1

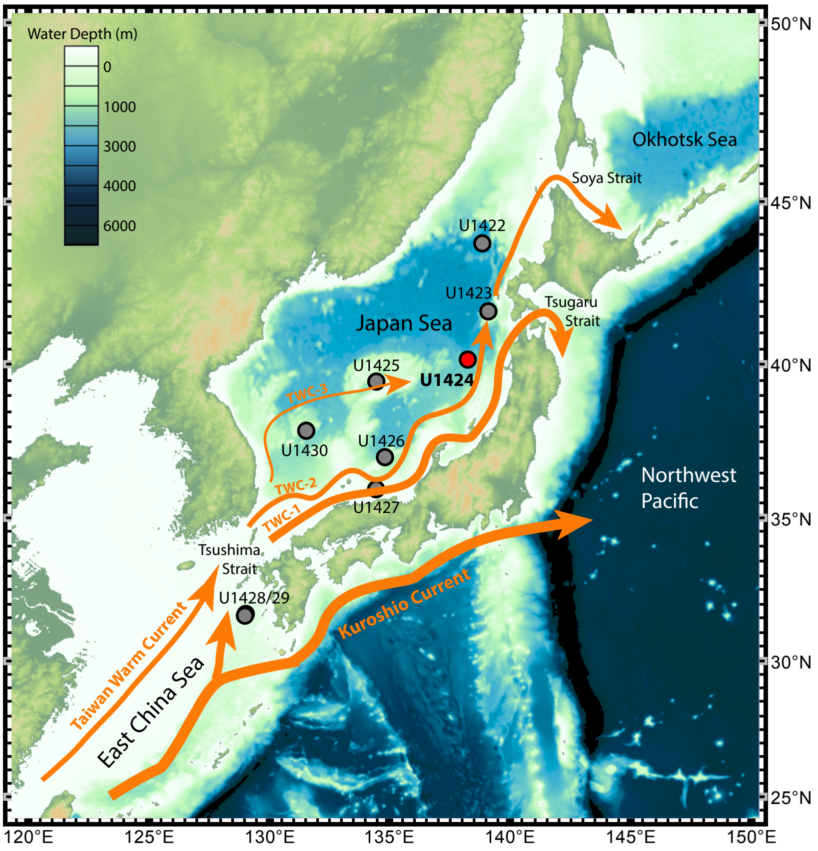
Water Depth (m)
0
1000
3000
4000
6000
Okhotsk Sea
Soya Strait
U1422
U1423
Tsugaru
Strait
Japan Sea
U1425
U1424
TWC-3
U1430
U1426
TWC-2
TWC-1
U1427
Northwest
Pacific
Tsushima
Strait
U1428/29
Taiwan Warm Current
East China Sea
Kuroshio Current
50°N
45°N
40°N
35°N
30°N
25°N
120°E
125°E
130°E
135°E
140°E
145°E
150°E

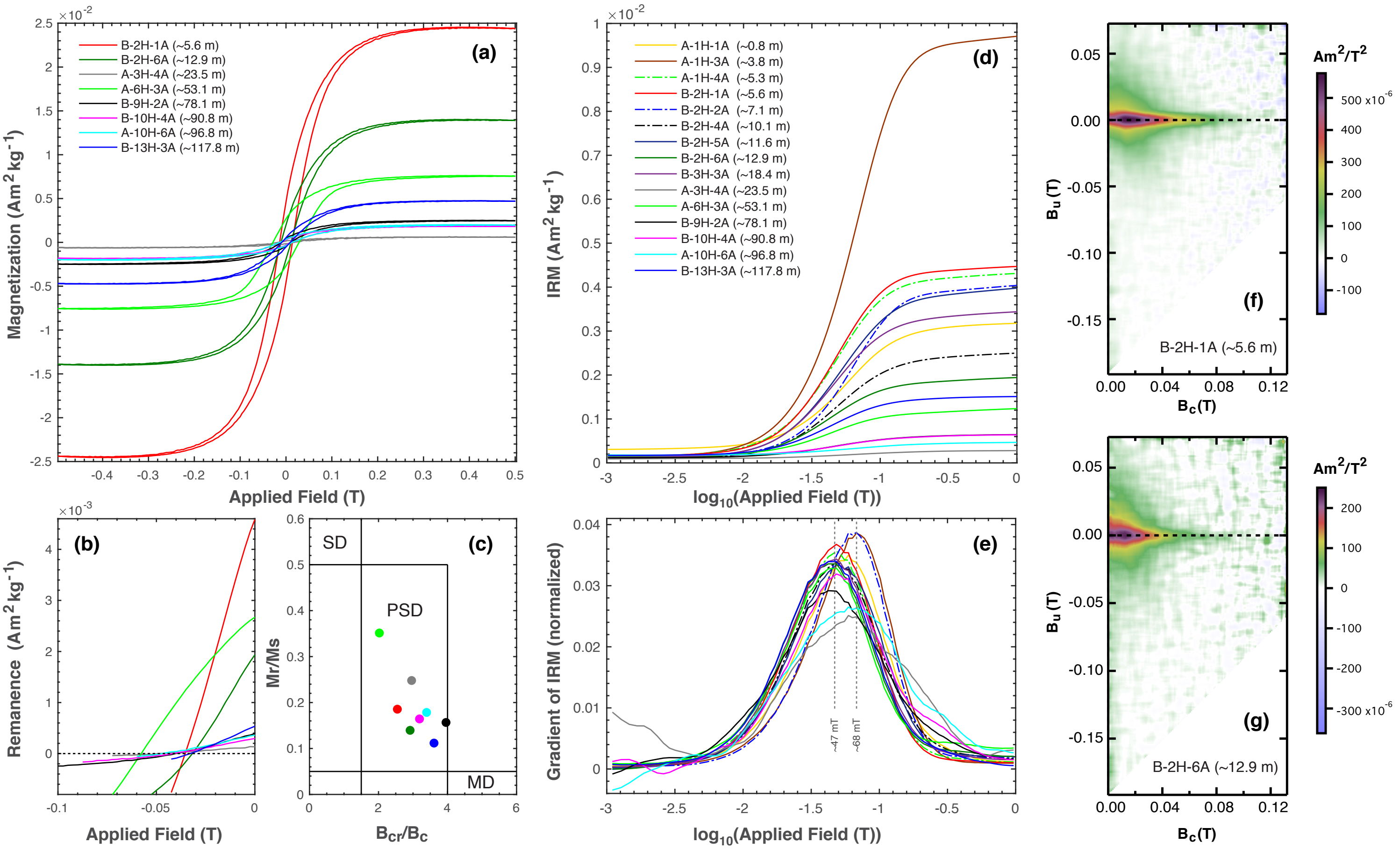
(a)
×10^-2
Magnetization (Am^2 kg^-1)
Applied Field (T)
B-2H-1A (~5.6 m)
B-2H-6A (~12.9 m)
A-3H-4A (~23.5 m)
A-6H-3A (~53.1 m)
B-9H-2A (~78.1 m)
B-10H-4A (~90.8 m)
A-10H-6A (~96.8 m)
B-13H-3A (~117.8 m)
2.5
2
1.5
1
0.5
0
-0.5
-1
-1.5
-2
-2.5
-0.4
-0.3
-0.2
-0.1
0
0.1
0.2
0.3
0.4
0.5
(d)
×10^-2
IRM (Am^2 kg^-1)
log10(Applied Field (T))
A-1H-1A (~0.8 m)
A-1H-3A (~3.8 m)
A-1H-4A (~5.3 m)
B-2H-1A (~5.6 m)
B-2H-2A (~7.1 m)
B-2H-4A (~10.1 m)
B-2H-5A (~11.6 m)
B-2H-6A (~12.9 m)
B-3H-3A (~18.4 m)
A-3H-4A (~23.5 m)
A-6H-3A (~53.1 m)
B-9H-2A (~78.1 m)
B-10H-4A (~90.8 m)
A-10H-6A (~96.8 m)
B-13H-3A (~117.8 m)
1
0.9
0.8
0.7
0.6
0.5
0.4
0.3
0.2
0.1
0
-3
-2.5
-2
-1.5
-1
-0.5
0
(f)
B-2H-1A (~5.6 m)
Bu (T)
Bc(T)
0.05
0.00
-0.05
-0.10
-0.15
0.00
0.04
0.08
0.12
Am^2/T^2
500 x10^-6
400
300
200
100
0
-100
(b)
×10^-3
Remanence (Am^2 kg^-1)
Applied Field (T)
4
3
2
1
0
-0.1
-0.05
0
(c)
SD
PSD
MD
Mr/Ms
Bcr/Bc
0.6
0.5
0.4
0.3
0.2
0.1
0
0
2
4
6
(e)
Gradient of IRM (normalized)
log10(Applied Field (T))
~47 mT
~68 mT
0.04
0.03
0.02
0.01
0
-3
-2.5
-2
-1.5
-1
-0.5
0
(g)
B-2H-6A (~12.9 m)
Bu (T)
Bc(T)
0.05
0.00
-0.05
-0.10
-0.15
0.00
0.04
0.08
0.12
Am^2/T^2
200
100
0
-100
-200
-300 x10^-6

Figure 3

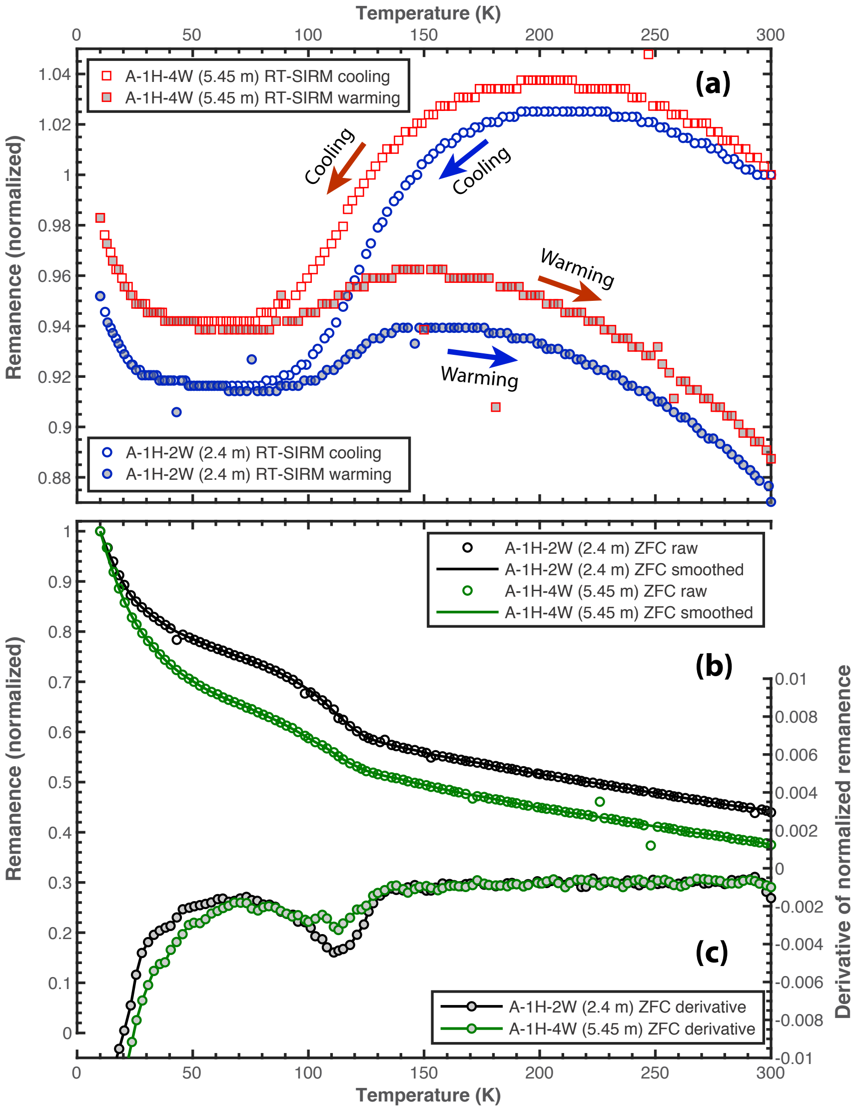
Temperature (K)
0
50
100
150
200
250
300
Remanence (normalized)
1.04
1.02
1
0.98
0.96
0.94
0.92
0.9
0.88
A-1H-4W (5.45 m) RT-SIRM cooling
A-1H-4W (5.45 m) RT-SIRM warming
(a)
Cooling
Cooling
Warming
Warming
A-1H-2W (2.4 m) RT-SIRM cooling
A-1H-2W (2.4 m) RT-SIRM warming
Remanence (normalized)
1
0.9
0.8
0.7
0.6
0.5
0.4
0.3
0.2
0.1
0
A-1H-2W (2.4 m) ZFC raw
A-1H-2W (2.4 m) ZFC smoothed
A-1H-4W (5.45 m) ZFC raw
A-1H-4W (5.45 m) ZFC smoothed
(b)
0.01
0.008
0.006
0.004
0.002
0
-0.002
-0.004
-0.006
-0.008
-0.01
Derivative of normalized remanence
(c)
A-1H-2W (2.4 m) ZFC derivative
A-1H-4W (5.45 m) ZFC derivative
0
50
100
150
200
250
300
Temperature (K)

Figure 4

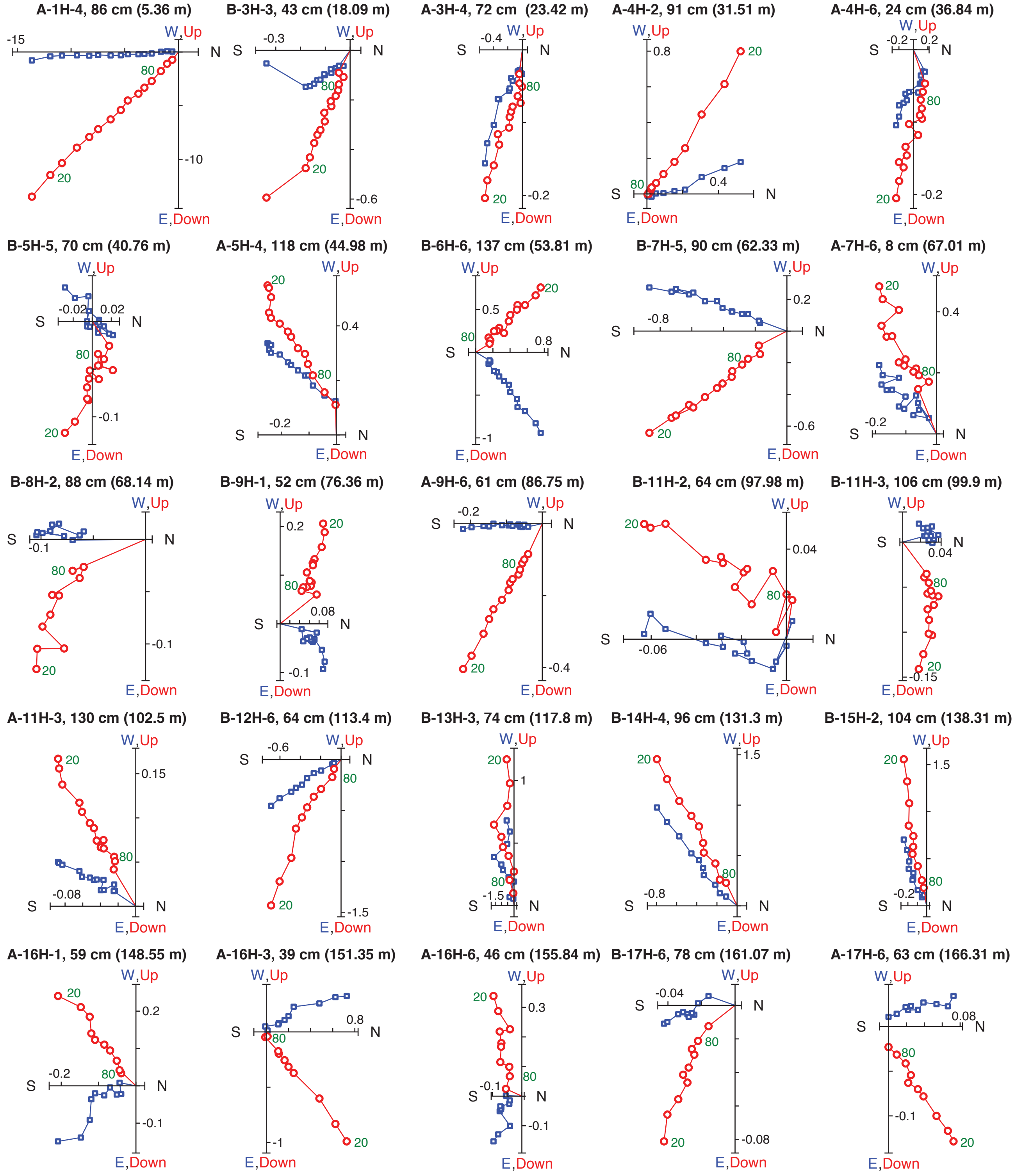
A-1H-4, 86 cm (5.36 m)
-15
-10
B-3H-3, 43 cm (18.09 m)
-0.3
-0.6
A-3H-4, 72 cm (23.42 m)
-0.4
-0.2
A-4H-2, 91 cm (31.51 m)
0.8
0.4
A-4H-6, 24 cm (36.84 m)
-0.2
0.2
-0.2
B-5H-5, 70 cm (40.76 m)
-0.02
0.02
-0.1
A-5H-4, 118 cm (44.98 m)
0.4
-0.2
B-6H-6, 137 cm (53.81 m)
0.5
0.8
-1
B-7H-5, 90 cm (62.33 m)
0.2
-0.8
-0.6
A-7H-6, 8 cm (67.01 m)
0.4
-0.2
B-8H-2, 88 cm (68.14 m)
-0.1
-0.1
B-9H-1, 52 cm (76.36 m)
0.2
0.08
-0.1
A-9H-6, 61 cm (86.75 m)
-0.2
-0.4
B-11H-2, 64 cm (97.98 m)
0.04
-0.06
B-11H-3, 106 cm (99.9 m)
0.04
-0.15
A-11H-3, 130 cm (102.5 m)
0.15
-0.08
B-12H-6, 64 cm (113.4 m)
-0.6
-1.5
B-13H-3, 74 cm (117.8 m)
1
-1.5
B-14H-4, 96 cm (131.3 m)
1.5
-0.8
B-15H-2, 104 cm (138.31 m)
1.5
-0.2
A-16H-1, 59 cm (148.55 m)
0.2
-0.2
-0.1
A-16H-3, 39 cm (151.35 m)
0.8
-1
A-16H-6, 46 cm (155.84 m)
0.3
-0.1
-0.1
B-17H-6, 78 cm (161.07 m)
-0.04
-0.08
A-17H-6, 63 cm (166.31 m)
0.08
-0.1
W,Up
E,Down
S
N
20
80

Figure 5

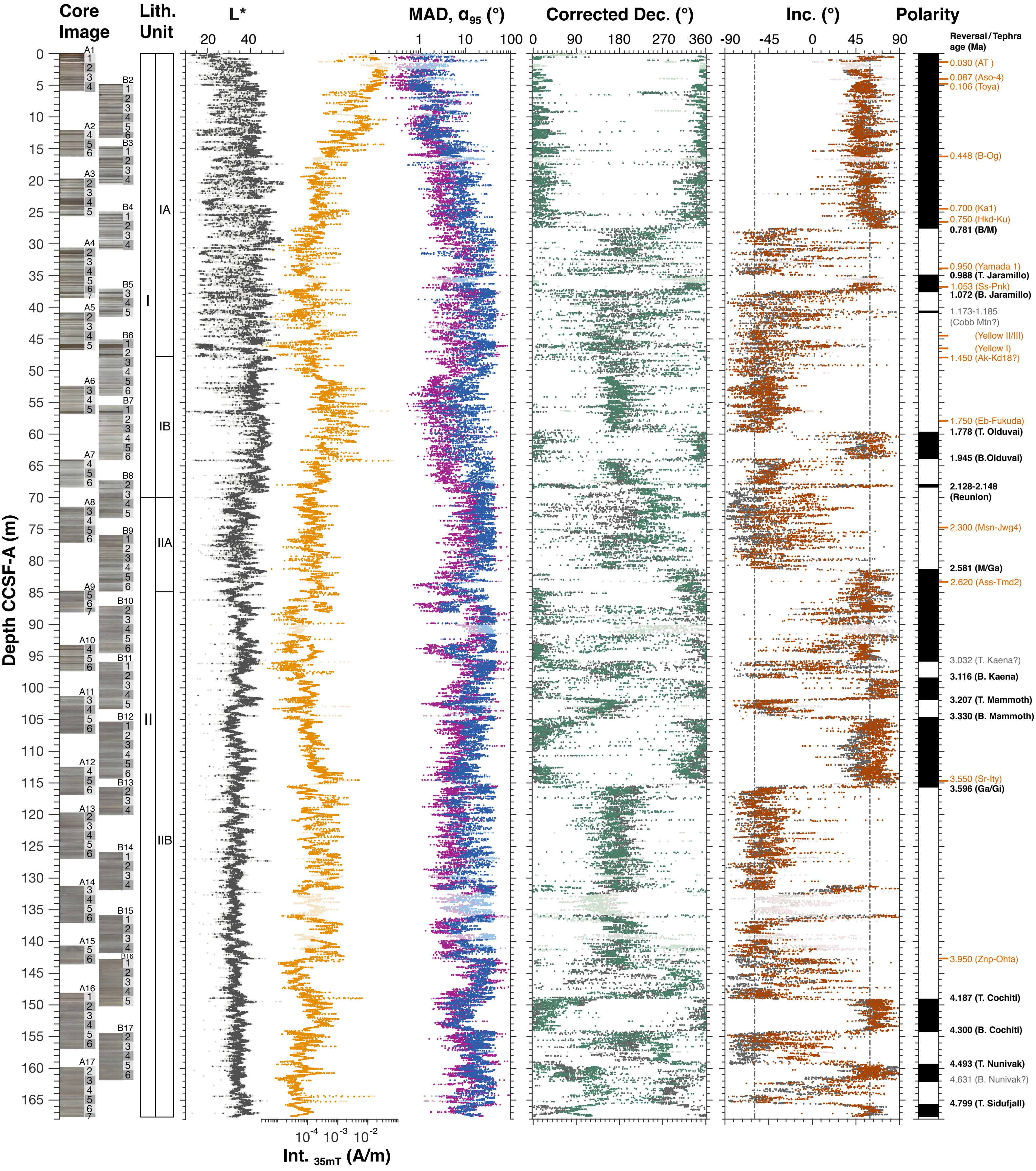
Core Image
Lith. Unit
L*
MAD, α_{95} (°)
Corrected Dec. (°)
Inc. (°)
Polarity
Reversal/Tephra age (Ma)
Depth CCSF-A (m)
Int. $_{35mT}$ (A/m)
10^{-4} 10^{-3} 10^{-2}
20 40
1 10 100
0 90 180 270 360
-90 -45 0 45 90
0 5 10 15 20 25 30 35 40 45 50 55 60 65 70 75 80 85 90 95 100 105 110 115 120 125 130 135 140 145 150 155 160 165
A1 A2 A3 A4 A5 A6 A7 A8 A9 A10 A11 A12 A13 A14 A15 A16 A17
B2 B3 B4 B5 B6 B7 B8 B9 B10 B11 B12 B13 B14 B15 B16 B17
I
II
IA
IB
IIA
IIB
0.030 (AT)
0.087 (Aso-4)
0.106 (Toya)
0.448 (B-Og)
0.700 (Ka1)
0.750 (Hkd-Ku)
0.781 (B/M)
0.950 (Yamada 1)
0.988 (T. Jaramillo)
1.053 (Ss-Pnk)
1.072 (B. Jaramillo)
1.173-1.185
(Cobb Mtn?)
(Yellow II/III)
(Yellow I)
1.450 (Ak-Kd18?)
1.750 (Eb-Fukuda)
1.778 (T. Olduvai)
1.945 (B.Olduvai)
2.128-2.148
(Reunion)
2.300 (Msn-Jwg4)
2.581 (M/Ga)
2.620 (Ass-Tmd2)
3.032 (T. Kaena?)
3.116 (B. Kaena)
3.207 (T. Mammoth)
3.330 (B. Mammoth)
3.550 (Sr-Ity)
3.596 (Ga/Gi)
3.950 (Znp-Ohta)
4.187 (T. Cochiti)
4.300 (B. Cochiti)
4.493 (T. Nunivak)
4.631 (B. Nunivak?)
4.799 (T. Sidufjall)

Figure 6

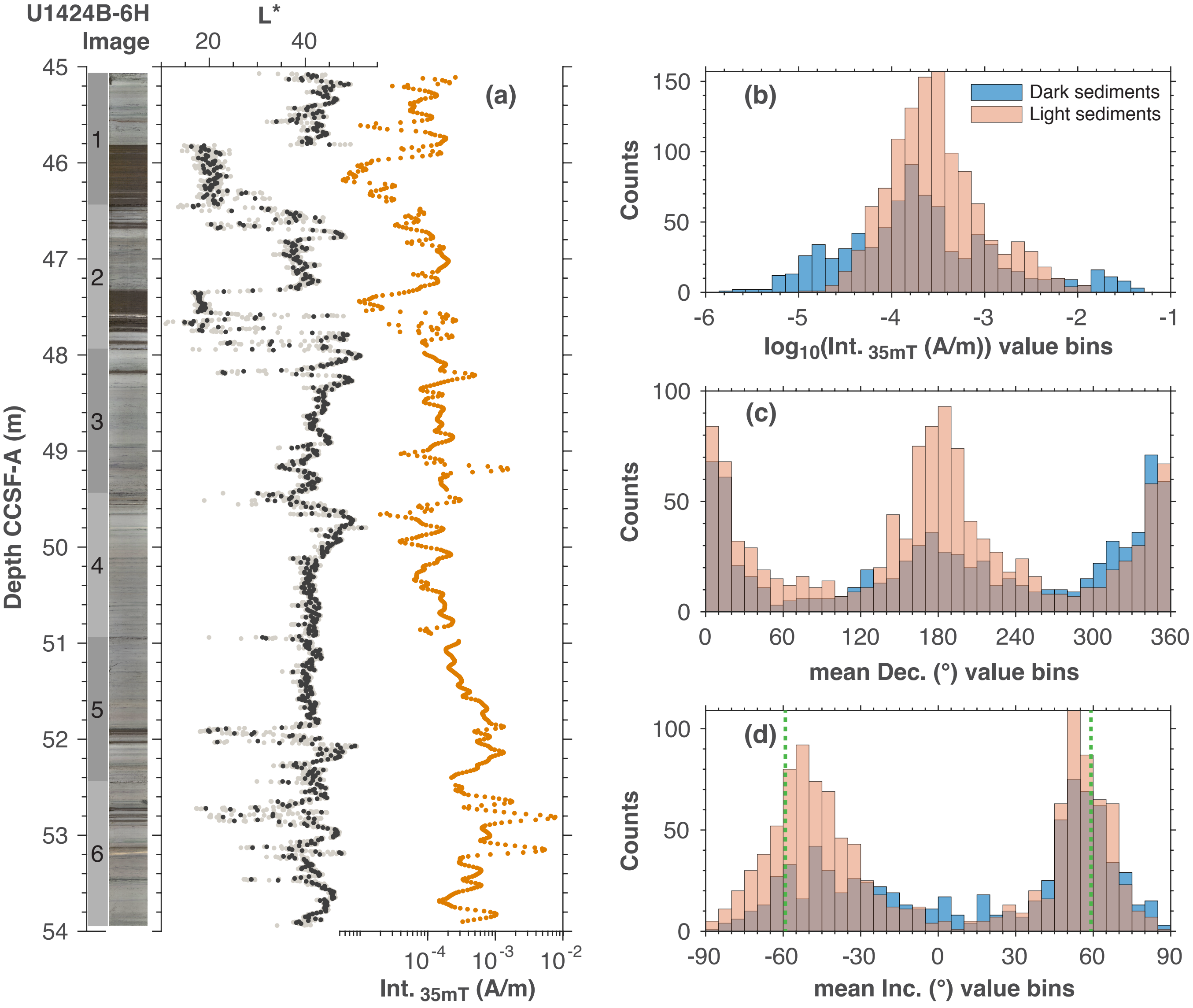
U1424B-6H
Image
L*
20
40
(a)
Depth CCSF-A (m)
45
46
47
48
49
50
51
52
53
54
1
2
3
4
5
6
10^{-4}
10^{-3}
10^{-2}
Int. 35mT (A/m)
(b)
Dark sediments
Light sediments
Counts
150
100
50
0
-6
-5
-4
-3
-2
-1
log10(Int. 35mT (A/m)) value bins
(c)
Counts
100
50
0
0
60
120
180
240
300
360
mean Dec. (°) value bins
(d)
Counts
100
50
0
-90
-60
-30
0
30
60
90
mean Inc. (°) value bins

Figure 7

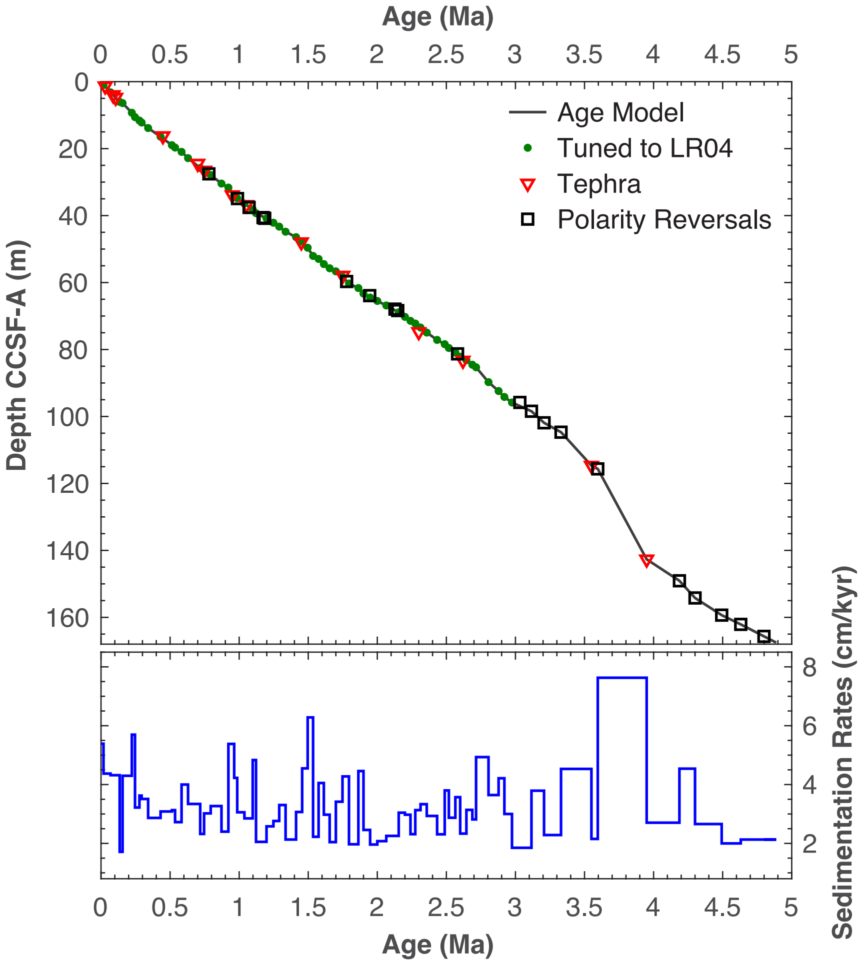
Age (Ma)
0
0.5
1
1.5
2
2.5
3
3.5
4
4.5
5
Depth CCSF-A (m)
0
20
40
60
80
100
120
140
160
Age Model
Tuned to LR04
Tephra
Polarity Reversals
Sedimentation Rates (cm/kyr)
2
4
6
8
0
0.5
1
1.5
2
2.5
3
3.5
4
4.5
5
Age (Ma)

Figure S1 (Part 1)

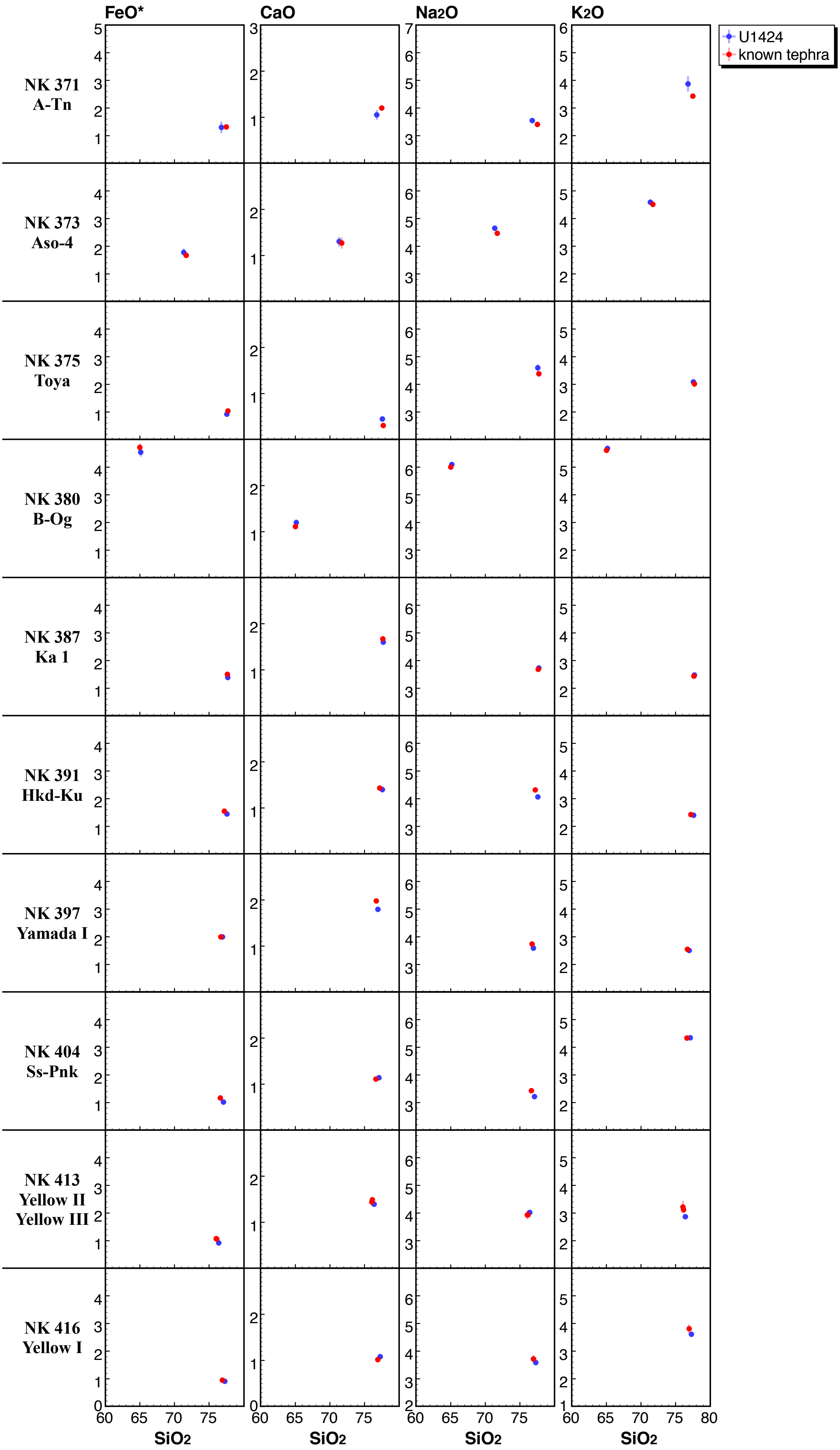

Figure S1 (Part 2)